

JGR Solid Earth

RESEARCH ARTICLE

10.1029/2021JB022699

Special Section:

Ophiolites and Oceanic Lithosphere, with a focus on the Samail ophiolite in Oman

Key Points:

- Geochemical profiles reveal continuous evolution of incompatible elements for the layered, and diverse fractionation for the upper gabbros
- REE and anorthite thermometry shows a homogenous temperature structure for the lower, and a variable temperature record for the upper crust
- Both suggests a hybrid model, with lower crust replenished in situ accretion and upper crust melt mixing and variable equilibrium dynamics

Supporting Information:

Supporting Information may be found in the online version of this article.

Correspondence to:

S. Müller,
samuel.mueller@ifg.uni-kiel.de;
mail.sam@gmx.net

Citation:

Müller, S., Garbe-Schönberg, D., Koepke, J., & Hoernle, K. (2022). A reference section through fast-spread lower oceanic crust, Wadi Gideah, Samail Ophiolite (Sultanate of Oman): Trace element systematics and REE crystallization temperatures—Implications for hybrid crustal accretion. *Journal of Geophysical Research: Solid Earth*, 127, e2021JB022699. <https://doi.org/10.1029/2021JB022699>

Received 28 JUN 2021

Accepted 24 FEB 2022




Author Contributions:

Conceptualization: Samuel Müller, Dieter Garbe-Schönberg, Jürgen Koepke
Data curation: Samuel Müller

© 2022 The Authors.

This is an open access article under the terms of the [Creative Commons Attribution-NonCommercial License](#), which permits use, distribution and reproduction in any medium, provided the original work is properly cited and is not used for commercial purposes.

A Reference Section Through Fast-Spread Lower Oceanic Crust, Wadi Gideah, Samail Ophiolite (Sultanate of Oman): Trace Element Systematics and REE Crystallization Temperatures—Implications for Hybrid Crustal Accretion

Samuel Müller¹ , Dieter Garbe-Schönberg¹ , Jürgen Koepke² , and Kaj Hoernle^{1,3}

¹Institute of Geosciences, Kiel University, Kiel, Germany, ²Institute of Mineralogy, Hannover University, Hannover, Germany, ³GEOMAR Helmholtz Centre for Ocean Research Kiel, Kiel, Germany

Abstract Oceanic gabbros are the most abundant rocks close to Earth's surface. Here we present new data from a consistent profile through the paleocrust of the Samail Ophiolite (Oman), which is thought to provide the best analog for modern fast-spreading oceanic crust. Incompatible trace elements of co-existing plagioclase and clinopyroxene fractionate from the mineral core to rim and up section from layered to foliated to varitextured gabbros. Layered gabbro parental melts correspond to mid-ocean-ridge basalts (MORB), and plagioclase Ca# shows a pronounced inverse zonation. Likely, they crystallized in situ from hydrous melts, compositionally buffered by replenishment at equilibrium to MORB and near steady-state boundary conditions. Further upsection, the compositional variability increases. Foliated gabbro rim and core compositions indicate increased fractionation and disequilibrium to MORB, triggered by open-system fractional crystallization within a heterogeneous magma plumbing structure, characterized by magma mixing, varying ambient water activities, and boundary conditions. Varitextured gabbros are chemically diverse with parental melts partially more primitive than MORB, suggesting that primitive melts directly reach the axial melt lens (AML). REE-in-plagioclase-clinopyroxene thermometry compared to and supported by anorthite-in-plagioclase thermometry reveals a relationship of $T_{\text{REE}}^{\text{An}} [^{\circ}\text{C}] = 6.1 \pm 0.2 \times \text{An} + 706 \pm 19$. Crystallization temperatures of the layered gabbros cover a narrow range of $1216 \pm 14^{\circ}\text{C}$. Considerable temperature variability of $1077\text{--}1231^{\circ}\text{C}$ is observed further upsection, featuring a thermal minimum within the foliated gabbros. This minimum is assumed to represent a zone where the fractionated descending crystal mushes originating from the AML meet with evolved liquids expelled from deeper crustal levels. Our findings suggest hybrid accretion of fast-spread crust.

Plain Language Summary Oceanic crust, the crystalline basement beneath the ocean-floor sediments is difficult to be sampled by shipboard drilling operations, but can be obducted onto continents by tectonic movement of lithospheric crustal fragments to form ophiolites. These rock formations serve as an analog to in-situ crust. They can be sampled along a profile from extrusive basaltic rocks to gabbros to the upper mantle giving access to the earth's interior. The geochemical and thermal evolution along a profile of paleocrust is crucial for gaining knowledge of the crust's accretional dynamics and formation processes. Our data suggest that the lower part the layered gabbros, are formed by a fundamentally different process than the upper foliated, and varitextured gabbros. While geochemical signatures systematically evolve upsection and the temperature structure is homogeneous for the lower part, the upper part is characterized by much higher dynamics and lower crystallization temperatures. Therefore, the crust forms in a hybrid process, where the lower part is dominated by near steady-state in situ crystallization in equilibrium with the parental melt. The upper part is formed in a more heterogeneous environment, dominated by subsiding crystal mushes, which mix with more primitive melts under disequilibrium conditions, yielding enhanced chemical variability.

1. Introduction

The formation processes and dynamics of fast-spread (-ing) oceanic crust are subjected to a long-standing scientific debate. Although more data on igneous oceanic lithologies became available over the last decades, a densely sampled coherent profile covering the full crustal range from the basaltic top down to the mantle is still missing, yet urgently needed since such a profile provides detailed insights on the accretional process of fast-spreading crust. Many studies have discussed diverse aspects on accretion of the oceanic crust: structural

Formal analysis: Samuel Müller

Funding acquisition: Dieter Garbe-Schönberg, Jürgen Koepke

Investigation: Samuel Müller, Jürgen Koepke

Methodology: Samuel Müller, Dieter Garbe-Schönberg, Jürgen Koepke

Project Administration: Dieter Garbe-Schönberg, Jürgen Koepke

Resources: Dieter Garbe-Schönberg, Jürgen Koepke

Software: Samuel Müller

Supervision: Dieter Garbe-Schönberg, Jürgen Koepke, Kaj Hoernle

Validation: Samuel Müller, Dieter Garbe-Schönberg

Visualization: Samuel Müller

Writing – original draft: Samuel Müller

Writing – review & editing: Samuel Müller, Dieter Garbe-Schönberg, Jürgen Koepke, Kaj Hoernle

and geochemical properties (e.g., Coogan, Gillis, et al., 2002; Coogan, Thompson, & MacLeod, 2002; Kelemen, Koga, & Shimizu, 1997; Pallister & Hopson, 1981; Pallister & Knight, 1981), melt migration dynamics through the mantle (e.g., Kelemen, Hirth, et al., 1997), crust-mantle boundary (e.g., Korenaga & Kelemen, 1997), and crust (e.g., Korenaga & Kelemen, 1998; Lissenberg & MacLeod, 2016; Lissenberg et al., 2013; MacLeod & Yaouancq, 2000), and properties of the crystallizing mush (e.g., Coogan & O'Hara, 2015; O'Hara & Mathews, 1981). With the more recent development in geospeedometry and geothermometry applied to gabbroic rocks (Coogan, Jenkin, & Wilson, 2002; Faak et al., 2013, 2015; Liang et al., 2013; Sun & Liang, 2017; Sun & Lissenberg, 2018) on the one hand and the development of numerical thermal models on the other hand (Cherkaoui et al., 2003; MacLennan et al., 2004, 2005; Theissen-Krah et al., 2011, 2016), the evaluation of the thermal structure of oceanic crust gets increasingly important and is subjected to a number of recent studies (e.g., Boulanger et al., 2020; Dygert et al., 2017; Faak et al., 2015; Sun & Lissenberg, 2018; VanTongeren et al., 2008). Our study sheds new light on ocean crust accretional dynamics by evaluating new geochemical data that gives insights into the variability of the crystallization regime along crustal depth and allows the evaluation of the in situ thermal structure of fast-spread oceanic crust. By focusing on primary magmatic features as a function of crustal depth, this work provides a direct link between the on-axis thermal rock record and numerical models of crustal accretion. This paper is part of a series of manuscripts that deal with different aspects of the Wadi Gideah transect sample suite obtained from the Oman ophiolite, which provides a coherent section through fast-spread oceanic crust (Garbe-Schönberg et al., 2022; Koepke et al., 2022; Mock, Ildefonse, et al., 2021).

1.1. General Dynamics at Fast-Spreading Ridge Systems

The oceanic crust formed at divergent plate boundaries makes two-thirds of Earth's near-surface rocks. These plate boundaries, the mid-ocean ridges, are characterized by sea floor-spreading and upwelling of the asthenospheric mantle, which undergoes adiabatic decompressional melting. This pressure release leads to a decrease of solidus temperatures below the ambient temperature of the upwelling mantle, resulting in partial melting of the mantle. The generated basaltic melt has a higher buoyancy than the surrounding mantle material and progressively ascends along a density gradient through the mantle and oceanic crust (e.g., Kelemen, Hirth, et al., 1997; Langmuir & Forsyth, 2007). A portion of the rising melt ascends to the surface. It erupts to form the extrusive rocks, mid-oceanic ridge basalt (MORB), as pillow and lobate lavas, sheet flows, and rare hyaloclastites (e.g., Perfit & Chadwick, 1998). When the melt becomes saturated with rock-forming phases as the temperature drops below the liquidus, it crystallizes within a near-surface melt lens, the AML, or in deep sills (e.g., Kelemen & Aharonov, 1998) to form the solid crust.

1.2. A Brief Inventory and Historical View on Oceanic Crust Sciences

After decades of efforts in the scientific Ocean Drilling Program (ODP) and International Ocean Discovery Program (IODP), direct access to deep fast-spreading crust is still limited to a few places on Earth (i.e., Hess Deep and related IODP drillings; Pito Deep from East Pacific Rise, EPR). Only one core, Hole 1256D in the eastern equatorial Pacific (Wilson et al., 2006), reflects a lithological series of intact fast-spreading oceanic crust, reaching from overlying sediments to basalts, sheeted dikes, and the topmost transitional (varitextured) gabbros. From Hess Deep, only relatively short drill cores exist from the deeper crust (layered gabbros and troctolites; Gillis et al., 2014). Moreover, a profile through the whole gabbroic crust was sampled via ROV (Lissenberg et al., 2013), but it is questioned whether this represents a coherent profile, due to the intense faulting associated with the Hess Deep intra rift setting (HDR; Francheteau et al., 1990). It was a breakthrough when the seismologically derived principal lithological layers of oceanic crust were found to match their lithological counterparts in fragments of oceanic lithosphere that had been obducted onto continents, forming ophiolites (Coleman, 1977; Glennie et al., 1973). Hence, these fragments could inevitably be identified to represent fossil oceanic crust, making ophiolites an ideal field laboratory for accessing gabbros of deeper crustal levels to gain insights into oceanic crust accretion and alteration dynamics based on their de facto stratigraphic order. The largest of these fragments, the Oman ophiolite (also referred to as Samail Ophiolite), is regarded as a fossil fast-spreading system (Boudier et al., 1997; Rioux et al., 2012) located in an oceanic setting influenced by subduction initiation (e.g., Guilmette et al., 2018), with basalts showing typical fore arc signatures (e.g., MacLeod et al., 2013).

1.3. Melt Dynamics and Proportions of the Crystal Mush at Fast-Spreading Ridge Systems

Melt flux at fast-spreading ridges is thought to be continuous, forming the crust in a near steady-state process. The upward migrating parental MORB melts are focused toward a region with a high melt proportion, as evidenced by the lack of propagation of s-waves in many seismological studies (Detrick et al., 1987; Hussenoeder et al., 1996; Wilcock et al., 1992). This region is called the axial melt lens (AML, or axial magma chamber, AMC, from some authors) and has a cross-axis lateral extent of a few hundred meters and a height of only a few tens of meters (e.g., Detrick et al., 1987; Kent et al., 2000). This region is situated beneath the sheeted dike complex (Nicolas et al., 2008) and laterally segmented along the axis (Babcock et al., 1998), building spreading cells (Carbotte et al., 2016) at varying crustal levels over time (France et al., 2009) and space (Carbotte et al., 2013). Beneath the AML follows a funnel-shaped zone of crystal mush, characterized by a reduced *P*-wave velocity (Dunn et al., 2000). This region spans the predominant part of the on-axis oceanic crustal column extending down to the mantle-crust transition zone (MTZ). The crystal mush zone (also called the magma plumbing system, by some authors) is likely subjected to a wide variety of spatially diverse combined crystallization, mixing, and reaction processes (O'Hara & Fry, 1996; O'Hara & Mathews, 1981; Sinton & Detrick, 1992). Despite the complex characteristics of such processes, the control on size, shape, and evolution of the crystal mush region is a function of the crust forming process and magma supply (Crawford & Webb, 2002). The melt fraction present in the mush is likely variable but generally increases toward the AML (Zha et al., 2014). While seismic tomography models estimate the amount of melt present at the base of the crust to only a few percent (Dunn et al., 2000), models using seafloor compliance measurements find a larger and more variable melt fraction of 5%–24% (Crawford & Webb, 2002; Crawford et al., 1999; Zha et al., 2014). This melt is likely stored in connected films or sills rather than in isolated pockets and has a residence time on a decadal time scale at fast spreading rates (Zha et al., 2014). It is essential to realize that the mush zone evolves as plate divergence proceeds and is heterogeneous in all dimensions with respect to density, viscosity, and temperature developing chemical gradients both from the lateral edge to the center and along the axis, and also vertically (Carbotte et al., 2013; MacLeod & Yaouancq, 2000).

1.4. A General View on Crustal Accretion

The seismological findings at in situ fast-spreading crust (e.g., Detrick et al., 1987; Wilcock et al., 1992) and the petrographic observations made for fast-spread paleocrust (e.g., Pallister & Hopson, 1981) gave birth to two very contrasting ideas on how to form oceanic crust. Both have distinct implications regarding the chemical evolution over depth and the crust's internal thermal structure. A successful model has to explain the lower crustal cumulate rock sequence. From MTZ to the AML: Modally layered gabbros with a layering parallel to the crust-mantle transition, followed by foliated gabbros that show a typical lineation steepening toward shallower crustal levels, in turn, followed by varitextured gabbros, which are regarded as the frozen fillings of the AML (Koepeke et al., 2022). In the gabbro glacier model (also referred to as ductile flow model), indicated by fabric pattern as described above, gabbros of the lower crust are regarded as cumulates from a top-down crystal mush flow that forms a gabbro glacier at the ridge axis flanks originating at the AML. In this model, the crust will not show significant internal differentiation and thermal variation since essential cooling is solely provided by the shallow hydrothermal convection system removing latent heat from the AML at steady-state crystallization conditions (Henstock et al., 1993; Quick & Denlinger, 1993). That the ductile flow model is problematic regarding the upward migration of melt was already shown by Korenaga and Kelemen (1998) and is emphasized in more recent studies (e.g., Lissenberg et al., 2013). The other end-member is the sheeted sill model (Kelemen, Koga, & Shimizu, 1997; VanTongeren et al., 2021), in which the plutonic section of oceanic crust forms via in situ crystallization (Langmuir, 1989) of sill-like intrusions into the deep crust. This model allows for differentiation along with crustal depth by the upward movement of fractionated and replenished, expelled melts. The sophisticated whole crustal magma chamber processes described by O'Hara and Mathews (1981) and O'Hara and Fry (1996) and the melt-rock interaction proposed by the in situ crystallization model (Korenaga & Kelemen, 1998) are recently studied in more detail (Coogan & O'Hara, 2015; Lissenberg & MacLeod, 2016; Lissenberg et al., 2013; Yang et al., 2019). The sheeted sill model requires a deep hydrothermal cooling system to remove the latent heat of crystallization in situ, allowing for thermal gradients along with crustal depth. In other words, the gabbro glacier model would always represent the conditions of the AML in the rock record and, therefore, should yield a constant and uniform crystallization temperature depth profile. The continuous evolution of melt up-section as proposed by the sheeted sills model along with dynamic cooling over depth would exhibit a temperature gradient from MTZ toward the AML that is shaped by the amount of crystallization and cooling provided to a certain

crustal level (Kelemen & Aharonov, 1998). The temperature profile over crustal depth is also modeled numerically by Cherkaoui et al. (2003) and by MacLennan et al. (2004, 2005) with results for the end member models as outlined above, but also combining the two formation mechanisms in a hybrid model with a temperature profile that features a thermal minimum within the foliated gabbros. This study aims to better understand the nature of crustal accretion by providing and evaluating a temperature-depth profile through the whole gabbroic crust formed at the fast-spread Oman paleoridge.

1.5. Refining the Crustal Genesis

Recent studies try to synthesize the ideas and observations as mentioned above and develop hybrid models where a gabbro glacier forms the upper crust, while the lower crust is formed by in situ crystallization (Boudier & Nicolas, 2011; Buck, 2000; Hopson, 2007; Jousset et al., 2012; Mock, Ildefonse, et al., 2021). Among many authors working on oceanic crustal accretion models, there is agreement that the upper-most part of the crust, the high-level gabbros (sometimes called isotropic gabbros and in this study referred to as varitextured gabbros), form as a result of crystallization within, or at the level of, the AML. For the subjacent crust, the genesis remains controversial. Obviously, the full spectrum of petrographic and geochemical properties so far discovered in oceanic gabbros (Coogan, 2014) cannot be the consequence of a single or uniform mechanism. As discussed by Coogan and O'Hara (2015) and Coogan and Dosso (2016), oceanic crust accretion is an open system process of a rather complex interplay between crystallization, magma mixing, and melt/rock interaction (see also MacLeod & Yaouancq, 2000), probably subjected to the influence of hydrothermal fluids at high temperatures (e.g., Bosch et al., 2004; Dygert et al., 2017; Gregory & Taylor, 1981; Nicolas & Mainprice, 2005; VanTongeren et al., 2008). Although closed system modeling approaches can explain the major geochemical trends of crustal evolution (e.g., Koepke et al., 2022), they fail to predict the full geochemical variety found in oceanic gabbros and therefore will not satisfy the three conditions for a successful accretion model as listed by Lissenberg and MacLeod (2016): (a) reproduction of the MORB compositional array, (b) consistency with the rock record, and (c) compatibility with constraints on mid-ocean ridge magma chambers. Because the MORB compositional array is quite large (Gale et al., 2013) and the rock record is variable for different parts of in situ crust (e.g., EPR) and for the Oman ophiolite (e.g., Coogan, Gillis, et al., 2002; Lissenberg et al., 2013; Perk et al., 2007), it is hardly possible to find a single unifying global solution for the magma chamber processes and accretion mechanisms involved in the formation of fast-spreading oceanic crust. Just recently, it has been discovered that the bathymetry and faulting at fast-spreading ridges can vary significantly within a few kilometers of the ridge axis (Maher et al., 2021). This is very likely a consequence of a variable magma supply along the ridge, showing that the underlying magmatic accretion system is likely to be variable on the scale of a few kilometers.

1.6. The Roll of Water, Hydrothermal Fluids, and Cooling

The Oman paleocrust and the EPR are often seen as analogous systems since they both feature a crustal profile of similar total thickness and spreading rate. Although direct, unbiased comparison of in situ fast-spreading crust and the Oman paleocrust is neither possible nor appropriate, magma will generally start to crystallize by crossing its liquidus temperature mainly controlled by composition but lowered as water content increases (Feig et al., 2006). Hence, the effect of water on the chemical and physical behavior of magma during differentiation has important consequences for melt transport, bulk fractionation, phase stabilities and equilibrium, and the resulting internal structure of the accreted crust. The Oman parental melt was elevated in water content (Koepke et al., 2021; MacLeod et al., 2013; Müller et al., 2017), very likely due to subduction initiation close to the Oman paleo spreading center. Nevertheless, temperature reduction is the driving force to initiate crystallization. Even at hydrous magmatic conditions, the latent heat of crystallization must be mined efficiently. Pure conductive cooling alone cannot account for this heat removal as the heat flow through gabbroic rock is insufficient, demanding a mechanism for convective heat transport to the hydrosphere. Gabbroic dikes and veins cutting the layered gabbro sequence and their associated phase assemblages have primary Sr-isotopic signatures influenced by seawater (Bosch et al., 2004). They may be formed along microcracks as a result of anisotropic thermal contraction during gabbro cooling, allowing for ingress of seawater at very high temperatures (Nicolas et al., 2003) and causing hydrous partial melting by the propagation of hydrous fluids along grain boundaries in the "just frozen" gabbros (Koepke et al., 2004; Koepke, Berndt, et al., 2014). Hence, elevated water activity is observed very close to the region of non-fully solidified gabbro. It was recently shown that highly charged hydrothermal fluids similar in

composition to black-smoker fluids are active within the lower oceanic crust (Zihlmann et al., 2018), with the potential to contribute to the mass and heat transfer budget from the deep crust to the oceans (Garrido et al., 2001; Koepke, Mueller, et al., 2014). In addition to the petrographic field evidence of fluids being active at high temperatures, active cooling of the lower crust can also be deduced from the thermal history of the rock record (Mock, Neave, et al., 2021; Sun & Lissenberg, 2018; VanTongeren et al., 2008) and structural observations (Mock, Ildefonse, et al., 2021; VanTongeren et al., 2015). Contrastingly, many studies find near conductive (slow) cooling rates (e.g., Coogan, Jenkin, & Wilson, 2002; Faak et al., 2015) for the lower crust. Due to the absent off-axis venting, the convective hydrothermal system is still believed to be mainly focused on the upper basaltic section of the crust, driven by the heat of the AML (Singh et al., 1999). Recently (Hasenclever et al., 2014) showed in a 3D numerical hydrothermal model that deep hydrothermal circulation can be coupled to the shallow circulation system without creating off-axis vent sites.

1.7. Geological Setting of the Oman Ophiolite and the Wadi Gideah Transect

The allochthonous Oman mountain range, situated along the east shore of the country, represents fragments of the Tethyan oceanic crust formed during the Cenomanian (Coleman, 1981) and obducted until the late Campanium (Searle & Cox, 1999). The mountain range can be divided into three structural units: the northern massif, the central massif, and the southern massif (Nicolas et al., 2000). It can be further subdivided into 12 blocks, from which each shows a more or less intact complete crustal profile. Unlike active fast-spreading ridges, the Oman ophiolite has a multi-stage magmatic history recorded both in the volcanic and in the gabbroic crust (Goodenough et al., 2010, 2014), dominated by two significant events commonly called magmatic stage one (V1) and magmatic stage two (V2; Godard et al., 2003; Rioux et al., 2012). While the first stage features a typical MORB-like magmatic signature related to the main formation phase of the crustal sequence, the second stage is dominated by signatures generally found in supra-subduction zone settings and relates to subduction initiation triggered magmatism. It is important to note that subduction-related magmatic influence is more substantial in the northern blocks and nearly absent within the southern massif. Our working area, Wadi Gideah, is located in the southernmost structural unit, the Wadi Tayin block, and is situated between Wadi Kadir to the West and Wadi Namara to the East, located about 10 km north of the town of Ibra (Figure 1a). It is part of the southern flank of the Wadi Tayin block where essential studies on the accretion, structural (Hopson et al., 1981; Pallister & Hopson, 1981) and geochemical (Pallister & Hopson, 1981; Pallister & Knight, 1981) properties, and isotopic systematics (Gregory & Taylor, 1981; Lanphere et al., 1981; Oeser et al., 2012) of oceanic crust have been carried out over the last decades. The Wadi Gideah drains southward from a divide a few hundred meters north of the crust-mantle transition. The divide has an average elevation of 1,060 m above sea level. Around the Wadi, the crustal section dips gently to the South, exposing a coherent series of crustal rocks with deeper crustal levels upstream to the North, and shallower levels downstream to the South, culminating in fossil submarine lava flows in the Ibra syncline (Pallister & Hopson, 1981). While gabbros and mantle rocks are well exposed along the Wadi, basalts, and sheeted dikes are generally only present as small hills within the lower Wadi plain. Based on field observations and structural data (Mock, Ildefonse, et al., 2021), the profile can be divided into the following units (from top to bottom): Axial melt lens, AML, ~5.0 km h.a.M. (height above the mantle-crust transition zone, for calculation of h.a.M., see Section 2.1), Varitextured gabbros, VG, ~4.1–5.0 km h.a.M., Upper foliated gabbros, UFG; ~3.5–4.1 km h.a.M., Lower foliated gabbros, LFG, ~2.6–3.5 km h.a.M., Layered gabbros, LG, ~0.2–2.6 km h.a.M., mantle-crust transition zone, MTZ, ~0–0.2 km h.a.M. (for details see Figure 1b, Koepke et al., 2022; Garbe-Schönberg et al., 2022; Mock, Ildefonse, et al., 2021). Varitextured gabbros outcrop north of the gabbro-dike transition zone at several hills roughly exceeding a height of 50 m, being widespread in the lower wadi plain, which is heavily covered by Neogene debris (Figure 1a). Foliated gabbros are found at the Wadi's mouth with a spatially diffuse transition over about 200 m toward layered gabbros exposed further upstream. Layered gabbros are the primary lithology in this area, outcropping along the Wadi flanks over a distance of approximately 6.5 km before merging into the mantle-crust transition zone (MTZ). This zone, covering up to 500 m in the Wadi bed, is characterized by intercalation of mantle, and lower crustal rocks, including decameter thick sequences of dunite. Up to the divide, harzburgite is exposed at very rough and steep terrains over roughly 1 km. Layering dips ~28° to the South, indicating a true crustal thickness of ~3 km for the layered gabbro series. The foliated gabbros further up section have a thickness of roughly 2 km, grading into the ~1 km thick horizon of varitextured gabbros before the plutonic sections ends with intermingled lithologies of the frozen AML (Müller et al., 2017) and the root zone of the sheeted dike complex (Nicolas et al., 2008). Throughout the Wadi, hydrothermal alteration zones can be

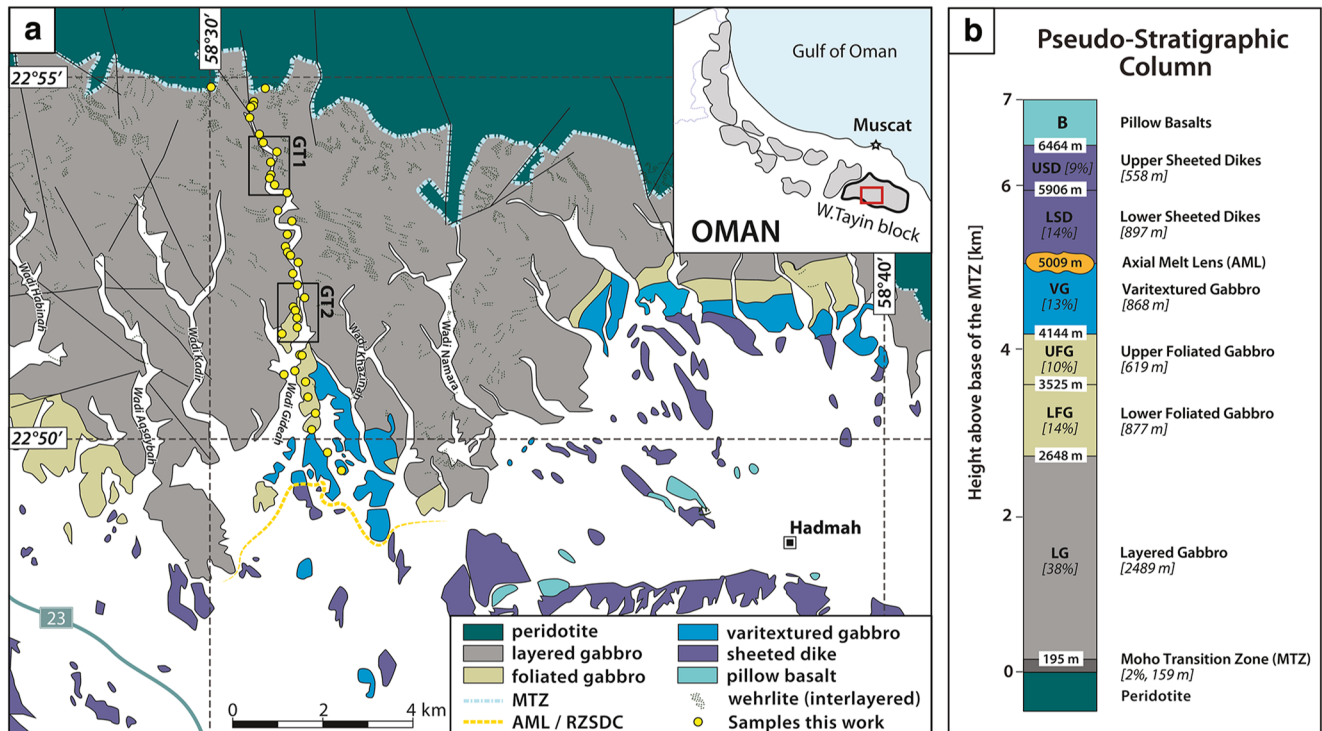


Figure 1. (a) Geological map showing the central part of the Southern Wadi Tayin ophiolite block in Oman, located about 10 km north of the town of Ibra. Sample locations along the Wadi Gideah transect are marked as yellow dots. (b) Lithological pseudo stratigraphic column of fast spread oceanic crust. Numbers in brackets represent the respective thickness and percentage in reference to the plutonic section, according to Mock, Ildefonse, et al. (2021). Separation between upper and lower sheeted dikes after Garbe-Schönberg et al. (2022). Geological map modified after (Peters et al., 2008). Wehrlites modified after (Nicolas & Boudier, 2015). Stratigraphic column modified after (Pallister & Hopson, 1981). B, basalts; USD, upper sheeted dikes; LSD, lower sheeted dikes; AML, axial melt lens; VG, varitextured gabbro; UFG, upper foliated gabbro; LFG, lower foliated gabbro; LG, layered gabbro; MTZ, mantle-crust transition zone. For details, see legend and text.

found in regular distances of about 0.5–2 km, crosscutting the layering of gabbros. These zones with a thickness of meters to decimeters are either isolated features or structurally more complex regions, consisting of highly altered, partially recrystallized gabbro (metagabbro), typically rich in chlorite, secondary amphibole, and oxides. They are similar to the focused fluid flow zones described by Coogan et al. (2006) for Wadi Namara and locally studied in detail for Wadi Gideah by Zihlmann et al. (2018).

2. Materials and Methods

2.1. Sample Materials From Wadi Gideah Transect

We have carefully selected 39 representative samples from the 230 samples of the Wadi Gideah Transect sample suite (Koepke et al., 2017; Müller, 2015), representing a full coherent crustal profile from MTZ to the dike/gabbro transition with an average sample spacing of about 120 m along the crustal depth. All samples were taken at outcrops of fresh gabbro along the Wadi. The height above the mantle-crust transition zone (h.a.M.) was calculated with respect to the MTZ reference latitude of 22.9152°N DD, assuming a generalized average dip of 28° for the layering of the lower gabbros in the Wadi Gideah area (Pallister & Hopson, 1981). The freshest and least altered region of each hand specimen was cut into a block with a water-cooled, diamond-blade saw, avoiding areas influenced by secondary weathering and hydrothermal overprint, and subsequently processed to a polished thin-section of 25–50 μ m thickness. We studied the samples using a polarized light microscope to identify petrographic key parameters and to select regions of interest suitable for microanalytical measurements based on the following conditions: (a) crystals and clusters belong to the primary rock-forming assemblage and domain, (b) have sufficient size to place multiple large spots in the core region when performing LA-ICP-MS measurements (spot size plagioclase 120 μ m, clinopyroxene 32–44 μ m), (c) homogeneous and well crystallized with smooth surfaces and with as few as possible cleavage cracks and fractures, and (d) showing the least amount of primary

(seafloor-related) and secondary weathering, metamorphic alteration and low-temperature hydrous overprint. All petrographic details can be found in the digital supplement (<https://doi.org/10.1594/PANGAEA.934706>).

2.2. Analytical Techniques, Data Handling, and Quality

The majority of major element mass fractions was measured at the Institute of Mineralogy of the University of Hannover using a Cameca SX100 electron microprobe operated through the Cameca PeakSight software. Additional data was generated at the Institute of Geosciences at Kiel University using a JOEL JXA 8900 R electron microprobe. Results from both labs have been cross-checked, analyzing identical samples. All elements have been measured at $K\alpha$ emission lines with a focused and fixed beam, an acceleration voltage of 15 kV, a beam current of 15 nA, and a signal count time per element of 10 s on peak and 5 s on each background. Matrix correction was performed following Pouchou and Pichoir (1991). For each of the 39 samples, repetitive measurements on multiple crystals were conducted. Although we put a strong focus on reliable primitive core measurements, we also acquired data for rim compositions from most samples. P -values have been calculated based on a paired, two-sided t -test to statistically evaluate the significance of the difference between core and rim mean mass fractions. If the p -value is small, the core-rim zonation is more significant (e.g., if the desired significance for the test is 95% which translates to an alpha level of confidence of 0.05, the zonation is significant if the p -value is smaller than the alpha value of 0.05). Additionally, propagation of uncertainty has been calculated for $Mg\# = Mg/(Mg + Fe) \times 100$ and $Ca\# = Ca/(Ca + Na) \times 100$. The K_2O mass fraction for most plagioclases is very low (~ 0.01 g/100g) and, therefore, doesn't affect the calculation of $xAn = An/(An + Ab + Or) \times 100$ beyond the propagated uncertainty of $Ca\#$, resulting in the absence of differences between $Ca\#$ and xAn .

For in situ analysis of 29 trace elements, carried out at the LA-ICP-MS lab of the Institute of Geosciences at Kiel University, a 193 nm ArF-excimer laser ablation system (GeoLasPro HD, Coherent) coupled to an Agilent 7900s ICP-MS was used for most samples. Some samples have been measured using an older Agilent 7500s ICP-MS, and a minor portion was measured using a Thermo Scientific Element XR ICP-SF-MS. In all cases, samples and reference materials were loaded into a Zuerich-type, two-volume low dispersion high capacity laser ablation cell (LDHCLAC, Fricker et al., 2011), which was flushed with 995 ml/min helium carrier gas. Additionally, 14 ml/min hydrogen was added upstream of the cell to enhance ionization in the ICP and reduce oxide formation. Many elements in plagioclase are within the ultra-trace mass fraction range (< 1 μ g/g). Therefore, the laser was operated at a high pulse frequency of 16 Hz and high fluence of 18 J/cm² with a crater size of 120 μ m for plagioclase. Clinopyroxene was measured at 10 Hz, 12 J/cm², and a crater of 44–32 μ m. We could not detect any adverse effects from mass load of the ICP for the elements determined. The oxide production rate was monitored by Th/ThO and kept below 0.1%. Time-resolved data acquisition for each measurement was split into 20 s background, 40 s sample ablation, and 20 s washout monitoring time. Dwell times were optimized for the expected mass fraction range for each element. Where possible, we aimed to perform five proximal repetitions for five crystals of each phase per sample to evaluate crystal core heterogeneity as well as sample phase heterogeneity.

The GLITTER software package was used for raw data reduction, applying initial calibration with NIST-SRM612 as the primary standard, using CaO g/100 g for the internal count to mass fraction reference. Potential errors from surface contamination have been avoided by excluding the first seconds of data acquisition from integration. The signal trace over time for each element (m/z) measured was checked for its analytical and geological reasonability and excluded in case of abnormal patterns or spikes (e.g., vertical transitions into different mineral phases during ablation, mineral inclusions, sulfide micro nuggets in clinopyroxene). A second, matrix-matched calibration step was realized by correcting against mean offset factors of median values from at least three repetitive measurements on nano-particulate pressed powder tablets (Garbe-Schönberg & Müller, 2014) of reference materials USGS-BHVO-2 (Jochum et al., 2016), USGS-BIR-1 (Jochum et al., 2016), and GSJ-JGb-1 (Garbe-Schönberg, 1993; Govindaraju, 1995; Imai et al., 1995; Jochum & Jenner, 1994; Jochum, Nohl, et al., 2005). All reference materials were analyzed multiple times for bracketing and drift correction throughout each analytical session. Some sessions have been calibrated against the USGS glass microanalytical reference materials USGS-BHVO-2G and USGS-BIR-1G (Jochum, Willbold, et al., 2005). Results of glass versus pellet reference materials show no significant difference and lead to similar correction factors. Analytical measurement uncertainties were found to be in the range of 1%–3% RMAD (1MAD) at mass fractions $> 10\times$ LOD for most elements analyzed. For monitoring systematic deviations from preferred or “true” values, the MPI-DING glasses GOR-128G, GOR-132G, and StHs6/80-G (Jochum et al., 2006) were measured as unknowns. Additionally, JF-1P with extremely low mass

fractions for most trace elements (Garbe-Schönberg, 1993; Govindaraju, 1995; Imai et al., 1995; Jochum & Jenner, 1994; Jochum, Nohl, et al., 2005; Kurosawa et al., 2006) was measured during most analytical sessions. Estimated deviations from preferred values of all analyzed reference materials are, for most elements, in the range of 5–10 RMSD% and within the uncertainties of the preferred or compiled values. All compositional data, reference values used in this study, literature sources, and data quality details can be found in the digital supplement (<https://doi.org/10.1594/PANGAEA.934706>)

2.3. Calculation of REE-In-Plagioclase-Clinopyroxene Temperature Densities

The thermometer of Sun and Liang (2017) uses a thermodynamic approach inferred from plagioclase and clinopyroxene lattice strain parameters to calculate crystallization temperatures based on phase equilibrium experiments where plagioclase and clinopyroxene crystallize from the same melt, making the melt composition obsolete for the calculation. Based on the hypothesis that plagioclase and clinopyroxene of oceanic crust are in equilibrium with the same melt (MORB), the melt itself can be neglected, and the thermometer can be used to calculate crystallization temperatures of oceanic gabbros with the consequence that the accuracy of calculated temperatures highly relies on the phase equilibrium. Therefore, the phase equilibrium needs to be checked in detail. This will be discussed in Section 4.3. The thermometer, however, basically derives two terms, $\ln(D_j)-A$ and B_j-1000 , from a modified version of the Brice equation (Brice, 1975). These terms incorporate the mineral composition, water content, and pressure into the calculation of crystallization temperature. The critical input parameter for the temperature calculation is the partitioning of REEs between plagioclase and clinopyroxene $D_{\text{REE}}^{\text{pl/cpx}}$. Although petrographic indications, for example, poikilitic textures of prismatic crystals with smooth grain boundaries that show no signs of reaction, suggest cogenetic crystallization, there is a priori no reasoning to assume or deny equilibrium between plagioclase and clinopyroxene cores based on their spatial distance at the scale of a thin section since plagioclase and clinopyroxene must be assumed to be mobile within the crystal mush. For this reason, paired calculation of $D_{\text{REE}}^{\text{pl/cpx}}$ is meaningful for rim compositions where the assemblage directly suggests cogenesis but not relevant for core compositions where the cogenetic equilibrium between individual plagioclase and clinopyroxene crystals is doubtful. Therefore, we calculated the outer matrix division of all spots analyzed in cores for each of the two phases within a sample, generating a matrix including all possible combinations of $D_{\text{REE}}^{\text{pl/cpx}}$. The resulting number of data points is therefore equivalent to $n_{\text{pl}} \times n_{\text{cpx}}$ (e.g., $n_{\text{row}} \times n_{\text{column}}$ of the matrix), and at each coordinate of the matrix, a unique value for $D_{\text{REE}}^{\text{pl/cpx}}$ is generated. This allows us to calculate temperatures for each partition coefficient individually, mapping the full data set produced by LA-ICP-MS to temperature. In other words, instead of narrowing the analytical information down by calculating medians of mineral core compositions, we exploded the data set to a matrix of plagioclase and clinopyroxene to get a better impression of the range of possible variations of $D_{\text{REE}}^{\text{pl/cpx}}$. The resulting data is expressed as a temperature kernel density distribution and discussed in detail in Section 4.5. This distribution represents not only the apparent temperature with the highest mode (or median if calculated so) of a sample expressed by the distribution's maxima but gives the potential spread of temperature recorded in a sample by assessing the distribution shape and width. This procedure generates a more detailed picture than performing the calculation based on average values.

For regression of the temperature inversion, we wrote a custom R script (<https://doi.org/10.5281/zenodo.5702686>) calling the MASS::rlm function (Venables & Ripley, 2002) to perform an iterated re-weighted least squares (IWLS) robust linear fit between REEs in the $\ln(D_j)-A$ and B_j-1000 space calculated following Sun and Liang (2017). For visualizing the inversion, median values for $\ln(D_j)-A$ were used. The resulting temperature of an individual sample is the median of the temperature density distribution and bound to two significant variances: (a) the standard error of the robust fit of REE-Y between $\ln(D_j)-A$ and B_j-1000 and (b) the distributions temperature range generated by the outer matrix $D_{\text{REE}}^{\text{pl/cpx}}$ space of each sample (Figure 2 and Figure S1 in Supporting Information S1). In other words, the regression performed here is robust against extreme values (e.g., Eu) and generates a more confident fit than conventional linear regression methods. In any case, the confidence interval of the regression (here expressed as standard error) gives the error of the calculated temperature in relation to the variance of input data and calibration of the thermometer. Nevertheless, the more important information we gain is the second variance of temperature, which represents the spread of temperatures recorded in the sample by performing individual calculations for the $D_{\text{REE}}^{\text{pl/cpx}}$ that yield the highest and lowest temperature, respectively. Additional variance on the calculated temperature comes from the analytical uncertainty and inaccuracy of major and trace element data, from inaccuracy of the thermometer's calibration and the depth-pressure model, as well as the assumption of water content in the temperature versus differentiation space.

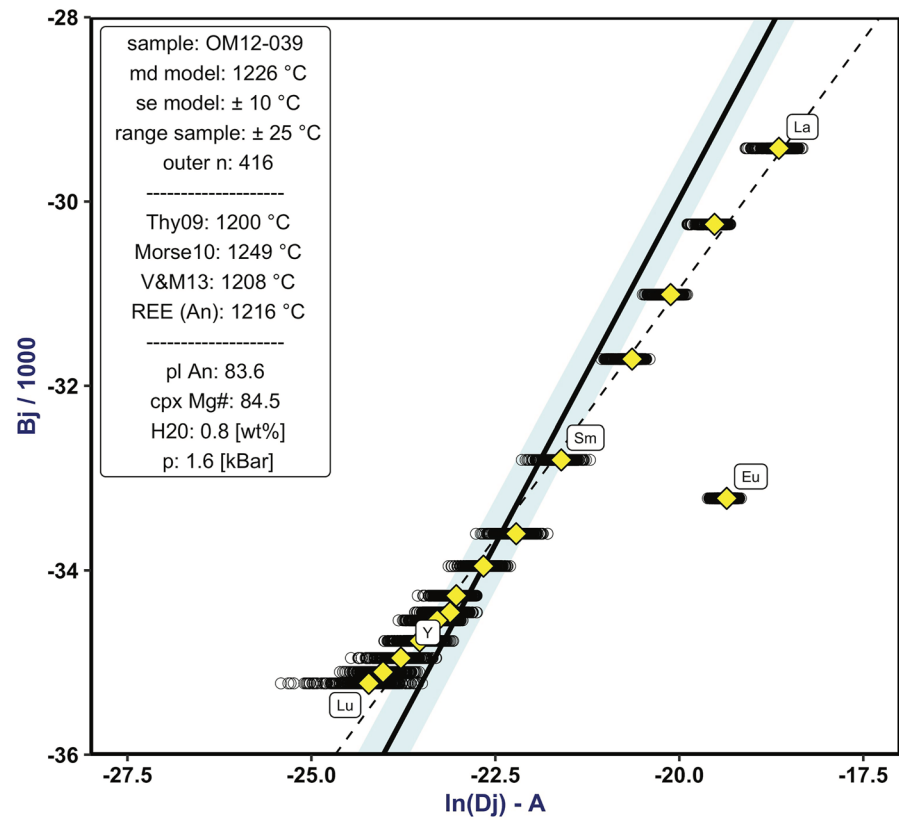


Figure 2. REE-in-plagioclase-clinopyroxene temperature inversion based on calculations following Sun and Liang (2017) for sample OM12-039 (LG, 1.3 km h.a.M.). The slope of the robust iterated re-weighted least squares (IWLS) linear regression (solid black line) through median values of $B_j - 1000$ and $\ln(D_j) - A$ (yellow diamonds) and forced through the origin of the parameters represents the near-liquidus crystallization temperature. Boundary parameters are shown in the white box. $D_{REE}^{pl/cpx}$ calculated by forming the outer matrix division of all spots analyzed per sample (black circles). The two errors bound to the median temperature (slope of the regression) arise from the standard error of the linear model (se model) and temperature spread caused by the sample's compositional variability (range sample), respectively. For comparison, three anorthite-based temperatures and the T_{REE}^{An} (cf., Figure 8) have been calculated: Thy09 (Thy et al., 2009), Morse10 (Morse, 2010) V&M13 (VanTongeren & Mathez, 2013). REEs are rotated against the thermometer's regression trough origin (dashed black line, not forced through the origin). For details, see methods Section 2.3 and discussion in Section 4.4 and Figure 8.

The calculation was tested for a constant pressure of 0.2 and 2 kbar over the full crustal depth and a continuous pressure gradient from 2 kbar at the MTZ to 0.5 kbar at the AML. Although these low pressures have no significant influence on the calculated temperatures ($\Delta P \sim 1^\circ\text{C}/\text{kbar}$ @ 1 kbar & 1 wt% H_2O , Figure S2 in Supporting Information S1), we decided to choose the latter model, as it reflects the true pressure conditions most precisely. The water content is mainly controlled by two parameters: (a) initial water content of the MORB melt and (b) incompatibility-driven enrichment of water in the melt by differentiation. A third possible component is the interaction of seawater with MORB melt by deep hydrothermal circulation, but little is known about that interface. Hence, the water content is challenging to be estimated precisely. Therefore, we choose a water content of 0.8 wt% H_2O for all samples (for details, see discussion). A higher water content generally lowers the crystallization temperature ($\Delta \text{H}_2\text{O} \sim 5^\circ\text{C}/\text{wt\%}$ @ 1 kbar & 1 wt% H_2O , Figure S2 in Supporting Information S1) since the water content of the melt during early crystallization is unlikely to exceed 1 wt% H_2O this effect on the temperature calculation is insignificant. As shown, pressure and water content only marginally influence the result of these calculations and are, therefore, of minor importance in relation to the geochemical variations. Since we see a general misfit in the results, where $T_{LREE} > T_{REE} > T_{HREE}$, temperatures for both LREE (La to Gd) and HREE (Tb to Lu) have been calculated separately to be compared to the overall fit and the median temperature. This situation arises from a rotation of the measured data against the calibration of the thermometer. Since the pressure term is lumped into the coefficient B and the water content is lumped into the coefficient A, regression over

REEs in the $\text{Ln}(D_j)\text{--}A$ and $B_j\text{--}1000$ space has to be forced through the origin (Sun & Liang, 2017). It has to be kept in mind that the calibration of the thermometer is intensely based on $D_{\text{LREE}}^{\text{pl/cpx}}$, since for $D_{\text{HREE}}^{\text{pl/cpx}}$ the database is sparse and might be inaccurate due to the very low mass fraction of HREEs in plagioclase. As a consequence, the overall calculated temperature might be too high if HREE $\text{Ln}(D_j)\text{--}A$ values are lower than the overall regression trend and are excluded from the fit. In other words, the exclusion of HREEs steepens the slope of the regression if HREEs are shifted toward lower $\text{Ln}(D_j)\text{--}A$ values and by that giving unrealistically high temperatures. This holds true vice versa for LREEs. For a more detailed picture concerning the applicability and reliability of the REE-in-plagioclase-clinopyroxene geothermometer, see discussion in Section 4.4.

3. Results

A set of 39 thin sections (26 layered gabbros, LG; 11 foliated gabbros, FG; and two varitextured gabbros, VG) from the 230 samples of the Wadi Gideah Transect sample suite were examined by transmitted and reflected light microscopy to obtain detailed information about modal proportions, grain sizes, accessory minerals, special textural features, and the degree of pervasive and vein-related alteration. Furthermore, plagioclase and clinopyroxene of all samples were analyzed in situ for major element mass fractions by EPMA and minor to ultra-trace element mass fractions by LA-ICP-MS. The general focus of this work is on core compositions of layered and foliated gabbros; rims were analyzed for some samples, but generally, plagioclase rims could not be measured for trace elements with the required small spot size due to the very low mass fractions of most elements. It should be noted that with only two varitextured gabbros present in our profile, this lithology is underrepresented. Still, these samples are representative of typical varitextured gabbros in Oman covering a range of compositions which is in good agreement with results of studies that explicitly deal with varitextured gabbros in Oman (e.g., Coogan, Thompson, & MacLeod, 2002). All petrographic and geochemical results can be found in the digital supplement (<https://doi.org/10.1594/PANGAEA.934706>).

3.1. Petrography and Composition of 39 Gabbroic Samples From the Wadi Gideah Crustal Transect

Most samples classify as olivine gabbro, but some are olivine-bearing gabbro or gabbro. Layered gabbros typically show cumulus formation characteristics with mostly medium-grained, subhedral to anhedral, granular textures with strong planar foliation, often with poikilitic clinopyroxene. Orthopyroxene is mainly absent and, if present, only in limited modal amounts of <1%. Intergranular and interstitial late-stage magmatic assemblages are absent or very limited within the layered gabbros but increase upsection from the layered gabbro to foliated gabbro transition. For the upper foliated and varitextured gabbros, amphibole, as well as oxides, become more abundant. Textures for the uppermost gabbros are isotropic, often with varying grain sizes and textural domains (varitextured gabbro). From the middle foliated gabbros upsection, visual zonation is increasingly common and omnipresent for plagioclase of the topmost gabbros. Olivine, where present, is intensely fractured and partially altered to iddingsite and serpentine. Two types of alteration can be found in all samples: (a) vein- and crack-related, and (b) pervasive alteration (“foggy” and/or fractured plagioclase) mainly in the range of 1%–3% with a few exceptions of >50%. Along cracks and veins, plagioclase typically forms chlorite. Where clinopyroxene is part of the reaction, actinolite and rarely tremolite is formed besides secondary hornblende, indicating amphibolite to greenschist facies triggered by hydrous overprint. This study focuses on the microanalysis of plagioclase and clinopyroxene, with details shown in the following.

3.1.1. Plagioclase

Anhedral to subhedral, rarely euhedral plagioclase has a modal proportion of 46–68 vol.%. Petrographically visible zonation is not observed within the layered gabbros, but an increasing drop in extinction angle for plagioclase rims in foliated and varitextured gabbros is apparent. Zonation is most intense in the center of the foliated gabbro level, being mostly continuous to oscillating. Plagioclase of Wadi Gideah gabbros contains 13–18 wt% CaO, 1.5–4.5 wt% Na₂O, and a maximum of 0.08 wt% K₂O. Ca# of plagioclase shows a significant difference between the lower and upper crustal ranges (Figure 3a). Within the layered gabbros, the average Ca# is 83 ± 1.7 and very uniform. For the foliated gabbros, Ca# is more variable and spans a range from ~55 to 82. Based on t-statistics, crystal rims of plagioclase tend to have a low (+0.02) but often significant enrichment of Ca relative to cores within the layered gabbros. This changes for the foliated and varitextured gabbros, where $\text{Ca}_{\text{rim/core}}^{\#}$ variations are more variable and pronounced for some samples with rims showing a significant depletion (−0.1) over cores

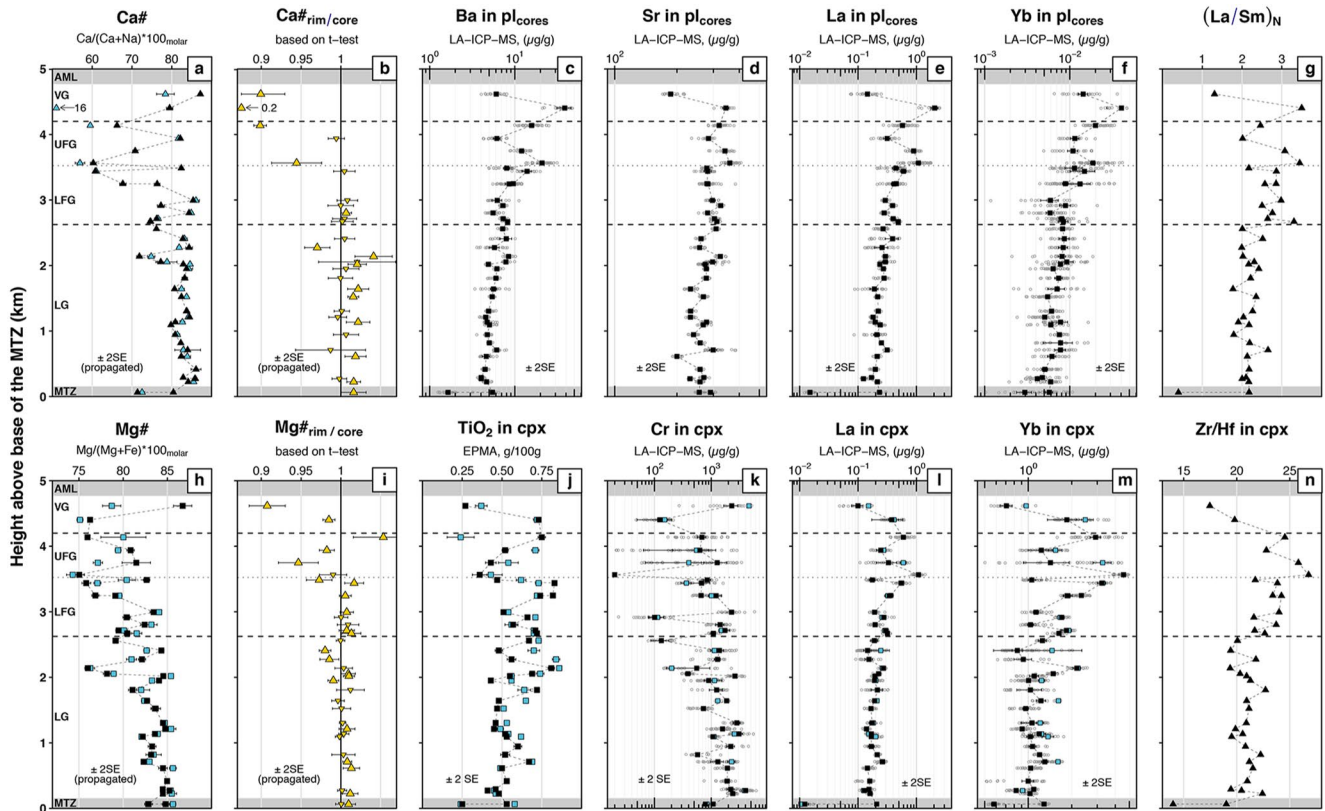


Figure 3. Geochemical evolution of plagioclase (top row) and clinopyroxene (bottom row) as a function of crustal depth (expressed as height above the MTZ, h.a.M.). Core analyses are in black and rim analyses in blue; individual measurement spots are presented as gray dots. (a) $\text{Ca\#} = (\text{Ca}/(\text{Ca} + \text{Na})) \times 100$. (b) Rim divided by core for Ca\# , as calculated from t -test statistics. Rim to core differences of $<99.5\%$ are considered meaningless (triangles pointing downwards). Note the often significant inverse zonation. (c–f) Median values for incompatible trace elements Ba, La & Yb, and compatible Sr in plagioclase cores. While incompatible elements yield a moderate enrichment toward shallower crustal levels, compatible Sr is predominantly conservative. (g) Chondrite-normalized ratios of incompatible elements $(\text{La}/\text{Sm})_N$ show a significant difference between the layered and foliated gabbros. (h) $\text{Mg\#} = (\text{Mg}/(\text{Mg} + \text{Fe})) \times 100$ versus depth for clinopyroxene. (i) Rim divided by core for Mg\# . (j) TiO_2 concentration of clinopyroxene cores and rims. (k–m) Median values for incompatible La, Yb, and compatible Cr mass fractions in clinopyroxene cores and rims. (n) Zr/Hf in clinopyroxene broadly reflects a similar trend as $(\text{La}/\text{Sm})_N$ in plagioclase. For lithological units see Figure 1, for details, see text.

but lower or insignificant differences for other samples (Figure 3b). Four samples deviate significantly from these observations. Two samples close to the LG/FG transition zone (OM12-054, OM11-A21A) yield lower Ca\# values of 77.2 ± 1 and 71.9 ± 0.5 , respectively. While the first is a typical cumulus gabbro, the latter is an oxide gabbro. These samples are not specifically different in their plagioclase trace element signatures but in terms of clinopyroxene composition (see below) and their accessory mineral assemblage. The lowermost sample (OM10-A32, 0.064 km h.a.M.) has a significantly lower Ca\# of 71 ± 0.3 and contrasts in most other geochemical indices. It shows a substantial depletion in REEs and has highly depleted LREEs. This trend is to some extent shared by the uppermost sample of the transect (OM10-A13, 4.6 km h.a.M.), a varitextured gabbro, which has substantially lower REE mass fractions when compared to most foliated gabbros and the other varitextured gabbro from our sample set.

For most trace elements (REEs, HFSEs, transition metals), average mass fractions in plagioclase crystal cores are generally low. Rare earth elements and Ba show a constant normal trend of chemical evolution of about one magnitude increase in mass fraction up section (Figures 3c–3f). The spread of compositions for individual samples significantly varies and increases as mass fractions decrease. With few exceptions, single crystals and different plagioclase crystals of a single sample are more homogeneous in the layered gabbros but more variable in composition in the foliated and varitextured gabbros. Light REE fractionation expressed as $(\text{La}/\text{Sm})_N$ (normalized to chondrite, McDonough & Sun, 1995) has on average a value of 2 for plagioclase of layered gabbros and becomes more fractionated and variable within the foliated gabbros (2–3.7, Figures 3g and 4). Trace elements are generally more enriched within the foliated gabbros, but they share the primitive signature found for the layered

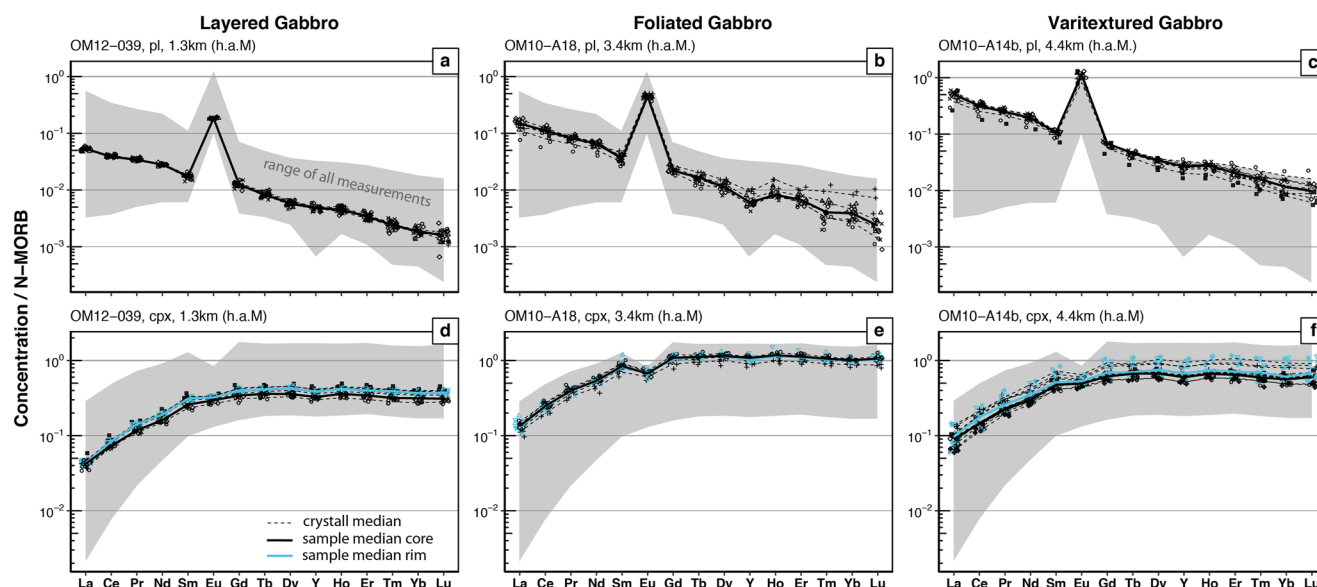


Figure 4. Crystal compositions of three representative samples from the different crustal units expressed as N-MORB normalized (Gale et al., 2013) REE profiles for plagioclase (left column) and clinopyroxene (right column). Individual analyses for different crystals (black for core, blue for rim; shapes correspond to individual crystals; no rim analyses for plagioclase), median compositions for individual crystals (dashed lines), plotted with respect to the full compositional range found in Wadi Gideah gabbros (39 samples, gray area). (a and d) The layered gabbro OM12-039 has a well-defined homogenous pattern (solid black line, average core composition per sample and phase) with only a little scatter of individual points of analysis or crystals. Average clinopyroxene rims (blue) are scarcely enriched over cores (black) for clinopyroxene. (b and e) Foliated gabbro OM10-A18 shows much higher mass fractions of REE + Y and an increased scatter around the crystals medians, especially for HREEs. It has to be noted that this scatter is not caused by analytical limitations (detection limit) but reflects a true feature of the investigated sample since much lower compositions could be measured with high precision. (c and f) Varitextured gabbro OM10-A14b has the most enriched pattern of the whole data set for plagioclase. Clinopyroxene REEs, on the contrary, are in the middle of the compositional range. Additionally, individual clinopyroxene rims are significantly enriched (blue symbols), while median compositions for rim and core are very similar. For details, see discussion.

gabbros in some cases. Overall, REEs in plagioclase have very consistent profiles (Figures 4a–4c). However, the variable fractionation behavior of LREE (cf., Figure 4b, rotation of REE curves for individual crystals) and HREE (cf., Figure 4c, variable HREE composition for individual crystals) represents crystal-unique features (e.g., dynamic processes on the grain-scale, small scale melt equilibrium variations). Hence, these features are only to a limited degree representative of the rock-forming processes.

3.1.2. Clinopyroxene

Modal proportions for clinopyroxene range from 25% to 49%, with a median amount of 33%. The shape is primarily anhedral to subhedral, rarely euhedral, with a granular, often poikilitic habit. Alteration of clinopyroxene is largely variable in the range of 1 to about 90%. It is mostly higher than the alteration of plagioclase of the same sample. On average, clinopyroxene cores within the lower layered gabbros are more uniform in their major to ultra-trace element composition than those further up section. Primitive layered gabbros show Mg# ranging from 81 to 85 (Figure 3h) and median TiO_2 of 0.52 ± 0.05 g/100g (Figure 3j). Mg# core-to-rim variations of clinopyroxene (Figure 3i) tend to reveal inverse zonation but, in contrast to plagioclase, associated with a lower significance. Rare earth elements vary only over a narrow range within the lower gabbros and show a moderate trend of enrichment from the MTZ toward the foliated gabbros (Figures 3l and 3m). Mass fractions of Cr in cores of clinopyroxene (Figure 3k) are elevated in the most primitive gabbros at the MTZ. Cr slightly decreases toward the layered to foliated gabbro transition zone, superimposed by high scatter ranging from about 400 to 5,000 $\mu\text{g/g}$. Zonation for Cr is variable with no clear trend of rim enrichment or depletion over crustal depth. Two samples (OM10-A21A, OM12-054) close to the layered gabbro/foliated gabbro transition zone are considerably more evolved, indicated by relatively low Mg# 76 and 78 that coincides with elevated TiO_2 of 0.81 and 0.69 g/100 g, respectively, and low Cr contents. They also have above-average HREE mass fractions (Figure 3m) but Zr/Hf signatures around 20 typical for primitive layered gabbros (Figure 3n). It has to be noted that OM10-A21A is an oxide gabbro.

For the foliated gabbros, Mg# in clinopyroxene extends to lower values and is more variable than in the crustal section below. Zonation being mostly normal (inverse for two samples) and more pronounced (Figures 3h and 3i) with a higher significance. TiO₂ shows a moderate trend of enrichment toward higher crustal levels with resets to very low mass fractions. Rims are partially enriched in TiO₂ but heavily depleted where Mg# is increased. REEs of foliated gabbros partially show strong enrichment but, like the major elements, also a considerable amount of scatter. In some samples, zonation is intense and in some cases covering a variety almost as large as the entire data set range (e.g., OM10-A17). Fractionation between incompatible elements Zr/Hf is substantially enhanced within the foliated gabbros (Figure 3m). The difference in composition between the two varitextured gabbros investigated here is a striking feature of the data set. The stratigraphically highest sample (OM10-A13, 4.6 km h.a.M.) has a very primitive but variable core composition of Mg# 86.7 ± 3.2 and fractionated rims of Mg# 78.7 ± 2.2 . Additionally, cores have very low TiO₂ of 0.27 ± 0.05 g/100 g and LREE mass fractions even lower than the average of layered gabbro clinopyroxenes. Rims are enriched in TiO₂ and incompatible trace elements (REE, Zr, Hf) but they have Cr contents similar to those of primitive layered gabbros ($\sim 2,000$ $\mu\text{g/g}$). The other varitextured gabbro (OM10-A14b, 4.4 km h.a.M.) generally shows the same core-to-rim systematics. However, it is substantially more evolved and homogeneous in major element composition, with core Mg# 76.3 ± 0.6 , TiO₂ of 0.74 ± 0.05 g/100 g, and low Cr mass fraction of ~ 140 $\mu\text{g/g}$.

4. Discussion

Two features of our new data set from Wadi Gideah gabbroic rocks are the inverse zonation of plagioclase within the layered gabbros and the presence of very primitive mineral compositions at the AML level, as found in one of the varitextured gabbro samples. These features will be discussed in Section 4.1 and Section 4.2, respectively. The main goal of this study is to gain a deeper insight into crustal accretion dynamics by combining geochemical characteristics with crystallization temperatures as a function of crustal depth by applying the novel REE-in-plagioclase-clinopyroxene geothermometer of Sun and Liang (2017). Since this geothermometer is directly based on the partitioning of REEs between plagioclase and clinopyroxene, it is crucial to test the samples for cogenetic equilibrium conditions. This will be assessed in Section 4.3. Subsequently, we will discuss the geochemical data and crystallization temperatures in the framework of crustal accretion processes.

4.1. Inverse Zonation of Plagioclase—Caused by Primitive Melt Injection or Water?

A striking feature of the Wadi Gideah layered gabbros is the tendency toward inverse zonation found in plagioclase Ca# and, to a more limited extent, in clinopyroxene Mg# (Figures 3b and 3i), a feature already observed by Müller (2015) and Koepke et al. (2022) for the whole sample set of the Wadi Gideah reference profile. In addition, although less systematic, this feature has been observed by Browning (1982) for a rhythmic series of layers in the Oman Wadi Shafan gabbroic complex and by Bosch et al. (2004) for a gabbro close to the MTZ in the Maqсад area. MacLeod and Yaouancq (2000) also report occasional reverse zoning in plagioclase for the upper gabbros. Nevertheless, systematic inverse zoning of plagioclase in oceanic gabbros to the extent observed in our samples is up to date not reported in gabbros from recent oceanic crust, implying that this is possibly a unique feature related to gabbros from the Oman ophiolite.

The cause of inverse zonation in the crystals is the presence of a compositionally different melt during rim crystallization. This melt either has to have a higher water activity, or it has to be more primitive. It has been shown experimentally (Berndt, 2002; Feig et al., 2006; Gaetani et al., 1993) that increased water activity leads to more anorthitic plagioclase compositions. In other words, $D_{\text{Ca-Na}}$ for the plagioclase melt equilibrium positively correlates with the water content. The effect of water activity on plagioclase composition depends on pressure and temperature. For lower crustal conditions (~ 2 kbar, $\sim 1100^\circ\text{C}$), the addition of only 1% H₂O can shift the plagioclase compositions by roughly 10% toward anorthite (Feig et al., 2006). In Oman, the water content of the initial melt was elevated (Koepke et al., 2021; MacLeod et al., 2013; Müller et al., 2017), explaining the generally more calcic nature of plagioclase in gabbros from Oman compared to those found at Hess Deep, where lower Ca# numbers are more common (Coogan, 2014). Therefore, water plays a key role during lower crustal crystallization and melt evolution. The formation of anhydrous olivine, plagioclase, and clinopyroxene from a wet melt allows for crystallization of hydrous phases at an early stage of differentiation and explains the systematic anorthite enrichment of the plagioclase rims. As a result of differentiation, the melt will also be slightly enriched in incompatible elements, which is reflected in elevated TiO₂ and Yb contents of the clinopyroxene rims (cf.,

Figures 3j and 3m). It should be noted that the water activity of the primary melts was variable, which is indicated by concordant wehrlite layers in coherent layered gabbro sequences of the OmanDP GT2 drill core (Kelemen et al., 2020b) and the reoccurring abundance of olivine melagabbro in the GT1 drill core (Kelemen et al., 2020a). The variable but repeated occurrence of interlayered wehrlites is additionally mapped by Nicolas and Boudier (2015) for the whole Wadi Tayin block (cf., Figure 1). In such layers, the corresponding parental melt batches were significantly enriched in water so that plagioclase was suppressed partially to produce olivine melagabbros or completely to form wehrlites (Koepke et al., 2009, 2021). Olivine data of the samples investigated here and discussion about ultramafic lithologies is beyond the scope of this paper but can be found in Koepke et al. (2022).

An additional water source is seawater-derived fluids. To date, there is no general agreement at what temperatures these fluids become active. While fast cooling rates (e.g., Sun & Lissenberg, 2018; VanTongeren et al., 2008) demand on-axis fluid systems active at an early accretion state, slow cooling rates (e.g., Faak et al., 2015) suggest no significant fluid contribution to the latent heat removal. In the latter case, the fluid system might develop slightly off-axis (Bieseler et al., 2018). From petrographic observations, it has been suggested that supercritical seawater can penetrate down to the MTZ and even into the upper mantle (Dygert et al., 2017) very close to the ridge axis via hydrothermal fault zones (e.g., Abily et al., 2011; Koepke, Mueller, et al., 2014; Rospabé et al., 2017; Zihlmann et al., 2018) or a microcrack system (Bosch et al., 2004; Nicolas & Mainprice, 2005). This can invoke hydrous partial melting and possibly enhance water contents of the primary melts by grain boundary transport to regions of active crystallization (Koepke, Berndt, et al., 2014). However, hydrous partial melting triggered by high-temperature fluids produced special micro-textures at the plagioclase grain boundaries and caused the precipitation of closely associated interstitial mafic phases (mostly pargasitic amphibole, e.g., Koepke et al., 2005a, 2005b; Koepke, Berndt, et al., 2014; Wolff et al., 2013), which were not observed in typical Oman layered gabbros away from hydrothermal fault zones. Moreover, deep hydrothermal activity reaching into the magmatic regime would be locally bound to pervasive hydrothermal faults and cannot account for such general zoning systematics recorded in the plagioclase. Additionally, the interface between the lower crustal high-temperature hydrothermal system and the magmatic regime is not well constrained.

A second option for explaining the inverse plagioclase zoning is the presence of heterogeneous, more primitive melt replenished into the crustal mush region where rim crystallization takes place. Recently it has been proposed for the Hess Deep magmatic system that melts intruding the crust before mixing and homogenizing within an eruptive reservoir have diverse compositions (Gillis et al., 2014). The intruding parental melt can be heterogeneous because the mantle is heterogeneous (Lambart et al., 2019) or due to a diverse multi-stage reaction history of the melts while crossing the MTZ. This is also known as the “reactive filter” hypothesis of MTZ formation (Abily & Ceuleneer, 2013). As shown geophysically, the Moho is neither a homogenous barrier between mantle and crust nor directly forms at the ridge axis center but rather successively increases in seismic reflection intensity until about 1 km away from the center of the ridge (Aghaei et al., 2014). Therefore, it is obvious that melt injected into the crust at the spreading center will differ in composition compared to melts injected slightly off the ridge axis center, where Moho formation and MTZ filtering increases. The lower crustal compositional variability found for the Wadi Tayin block has already been attributed to source melt heterogeneity by Pallister and Hopson (1981). However, given the distinct and in principle homogeneous geochemical character of the layered gabbros in Wadi Gideah, melt injection heterogeneities, independently of being the result of mantle heterogeneities or MTZ reaction history, are not likely to significantly influence the lower crustal primary accretion and internal chemical evolution. Since the crust has a high melt permeability (Zha et al., 2014) heterogeneous melt batches might be homogenized and replenished with fresh MORB melt before they intensely react with the already existing mush framework. Recent studies propose an enhanced influence of reactive porous flow and AFC processes on the evolution of the oceanic crust (e.g., Lissenberg et al., 2013; Sun & Lissenberg, 2018). A significant feature of reactive porous flow is the strong normal zonation of plagioclase, which for Wadi Gideah gabbros is only present within the UFGs and VGs, while in the lower crust (LFGs and LGs), inverse plagioclase zonation dominates. Additionally, it has to be noted that zoning in clinopyroxene, especially in the lower crust, is in general low and much less developed than the zoning reported by Lissenberg et al. (2013) for the Hess Deep EPR gabbros, implying that reactive porous flow in the Oman paleo crust played only a minor role. Instead, reactive textures present in the Oman layered gabbros are rather linked to hydrous partial melting instead of reactive porous flow (Koepke et al., 2022). This leaves differentiation-driven water enrichment as the most likely scenario causing the inverse zonation.

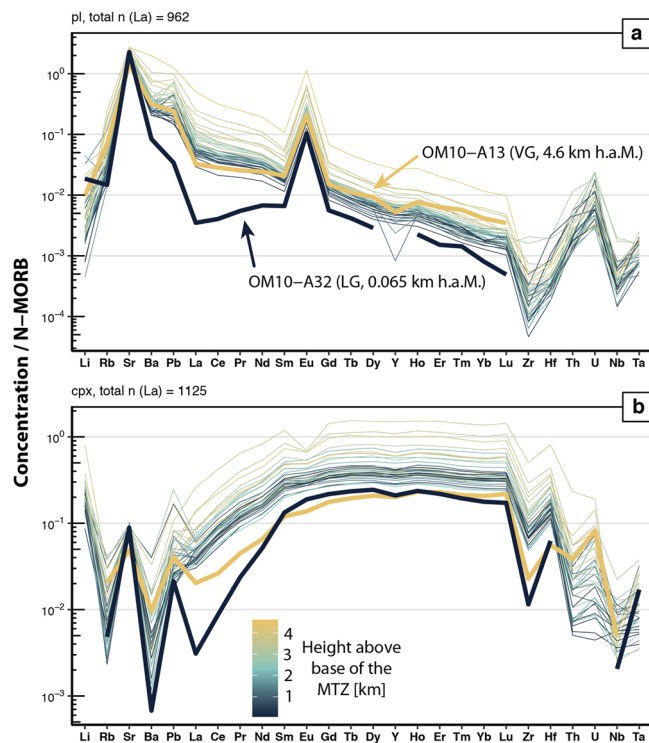


Figure 5. Trace elements spider plots of median values for all 39 samples; (a) for plagioclase and (b) for clinopyroxene (only core compositions). Line color corresponds to crustal depth (see legend, h.a.M., height above the mantle-crust transition zone). Two samples are highlighted: The lowermost layered gabbro (OM10-A32, dark blue line) and a varitextured gabbro (OM10-A13, orange line) from the AML horizon, bearing very primitive cores as relics. For details, see text.

what more evolved, showing that for very primitive melts, plagioclase is suppressed by increased water activity. This finding is remarkable in two aspects. First, it shows that melts are transported through the entire plutonic crust without losing their primitive signature. Second, although other studies from Oman find highly magnesian clinopyroxene and calcic plagioclase as cores in minerals from the varitextured gabbros (Coogan, Thompson, & MacLeod, 2002; Koepke et al., 2022; MacLeod & Yaouancq, 2000), the composition of sample OM10-A13 is among the most primitive ever found at the level of an AML, both in Oman (Garrido et al., 2001; Pallister & Hopson, 1981) and at in situ fast-spreading ridge systems, including the very primitive Pito-Deep samples (Lissenberg et al., 2013; Pedersen et al., 1996; Perk et al., 2007). These signatures hint toward melts that are possibly more primitive than the melts from which the layered gabbros have crystallized and more primitive than the most primitive erupted MORB (Figures S3 and S4 in Supporting Information S1). They are likely a mixture of UDM and more evolved liquids. Still, they have not substantially reacted with the lower crust crystal mush, implying that melt/rock interaction was low or non-existent, otherwise their primitive signature would have been blurred. The conventionally suggested locations where aggregation of primitive melt occurs are the uppermost mantle and the lowermost crust (Coogan, Gillis, et al., 2002). Here we show that extreme primitive melts have the potential to reach the AML, implying that initial aggregation of individual melts may also occur within the axial melt lens. Likely, they never erupt before mixing with evolved AML melts, explaining the absence of MORB as primitive as suggested by primitive rocks found at the AML crustal level. A similar conclusion is drawn by Costa et al. (2010) for the EPR. Wanless and Shaw (2012) estimated the crystallization depths of MORB phenocrysts. They show that about 75% of the investigated melt inclusion in olivines from MORBs from the Pacific crust crystallized in the environment of the AML horizon, which also demonstrates that the AML is a place where primitive MORB is delivered. Melts that have previously undergone little or no differentiation have to reach the AML in a marginal and widely isolated region that can be described as a central feeder channel, where boundary conditions

4.2. Primitive Melt Delivery to the AML—Evidence for a Central Feeder Channel?

The highest Ca# value of the whole data set is found in plagioclase cores of the uppermost sample (OM10-A13, 4.6 km h.a.M.), a varitextured gabbro. It has a Ca# of 87.2 ± 0.17 , much higher than the median of layered gabbros (83 ± 1.2) and also exceeds the most primitive layered gabbros (86.1 ± 0.66 ; Figure 3a). The same situation is found for Mg# in clinopyroxene, where cores for sample OM10-A13 also have the highest Mg# (86.7 ± 3.22 ; Figure 3b). Ratios of incompatible elements (La/Sm_N in plagioclase and Zr/Hf in clinopyroxene) are markedly lower than in all other samples. The Ce/Yb ratios of 27 for plagioclase and 0.6 for clinopyroxene are considerably lower than for all other samples, median ~ 80 and ~ 0.9 , respectively. Mass fractions of incompatible elements (TiO_2 , REEs in clinopyroxene, Ba, LREE in plagioclase) are close to the lowermost end of the data set, falling off the evolutionary trend depicted up section (Figures 3 and 5). Compatible elements (e.g., Cr in clinopyroxene) have elevated mass fractions. The depleted, non-fractionated REE characteristics of the parental melt for this sample (Figure S3 in Supporting Information S1) bears evidence for very primitive liquids ascending from the mantle source to high stratigraphic levels and into the AML. The clinopyroxene REE pattern of this sample corresponds to those from gabbro sills crystallized within the MTZ. They are characterized by very depleted LREEs (e.g., Sample OM10-A32, Figure 4; and Kelemen, Hirth, et al., 1997). Calculated equilibrium melts for these sills (OM10-A32, Figure S4 in Supporting Information S1) are not in equilibrium with Oman MORB but closely resemble the composition of ultra depleted melt (UDM) inclusions found as primary features in olivine of MORB (Sobolev & Shimizu, 1993), which additionally supports the argument of very primitive melts being fed directly into the AML. Although the equilibrium melt for clinopyroxene of the varitextured gabbro OM10-A13 is significantly more evolved than UDM, it features a notable depletion of LREEs typical for, and likely inherited from, UDM. The plagioclase pattern is some-

allow for crystallization of extreme primitive plagioclase and clinopyroxene. A similar conclusion was derived for varitextured gabbros drilled in the EPR crust at IODP site 1256 (Koepke et al., 2011).

4.3. Equilibrium Between Plagioclase, Clinopyroxene, and Oman MORB Melt

In order to calculate crystallization temperatures using the geo-thermometer of Sun and Liang (2017), the essential requirement of the sample is equilibrium between plagioclase and clinopyroxene. Only if they have crystallized from the same melt under equilibrium at constant boundary conditions, their calculated temperatures will be valid. Since petrographic evidence for interpreting equilibrium is always uncertain, we evaluated whether equilibrium was given by calculating the equilibrium melts based on measured compositions of plagioclase and clinopyroxene, applying distribution coefficients for mineral-melt partitioning. Subsequently, we checked whether the equilibrium melt compositions for plagioclase and clinopyroxene differ from each other or not and to what extent they resemble the Oman MORB compositional array (Garbe-Schönberg et al., 2022).

Partitioning coefficients for plagioclase have been calculated based on a recently parameterized lattice strain model provided by Sun et al. (2017). Required input parameters are not only major and trace element compositions but also pressure and temperature. The pressure sensitivity for REE partitioning in plagioclase is low and the pressure range for oceanic crust formation only varies from 2 kbar (MTZ) to about 0.5 kbar (AML) and, therefore, the pressure effect is negligible. The temperature, on the other hand, has a significant influence on REE partitioning in plagioclase and has to be chosen carefully. Here we used the geothermometer of VanTongeren and Mathez (2013), which is based on the anorthite content of plagioclase, to derive initial temperatures for the $D_{\text{REE}}^{\text{pl/melt}}$ calculation. A difficulty arises from the influence of water. As noted previously, an increase in water content leads to higher anorthite values ($\Delta \text{xAn} \sim 10 \text{ An/wt\% H}_2\text{O}$ @ 1100°C & 2 kbar, Feig et al., 2006; Koepke et al., 2004), resulting in higher anorthite-temperatures. Counterintuitively, $D_{\text{REE}}^{\text{pl/melt}}$ is positively correlated to the water content and negatively correlated to xAn (Bédard, 2006), which is somewhat conflicting since water content positively correlates to xAn. The reason for this might be that the role of water with respect to $D_{\text{REE}}^{\text{pl/melt}}$ is experimentally not well constrained and shows a rather crude correlation (e.g., Equation 44e of Bédard, 2006), conclusively the influence of water on $D_{\text{REE}}^{\text{pl/melt}}$ is much lower than on xAn. Knowing that the Oman source melt had a notable amount of water (MacLeod et al., 2013; Müller et al., 2017), the approach of using water content-dependent temperatures (VanTongeren & Mathez, 2013) in the calculation of $D_{\text{REE}}^{\text{pl/melt}}$ following Sun et al. (2017) has to be treated with caution but still yields more plausible values for the partitioning than applying the regression-based parametrization of Bédard (2006).

For clinopyroxene $D_{\text{REE}}^{\text{cpx/melt}}$ were calculated following Bédard (2014), using the nearest neighbor regression flow-chart method. $D_{\text{REE}}^{\text{cpx/melt}}$ values correlate well with each other ($R^2 > 0.9$), therefore the REE + Y internal D relations are reliable. The difficulty then only lies in picking a procedure to calculate the $D_i^{\text{cpx/melt}}$ for the introduction point (i.e., Samarium, $D_{\text{Sm}}^{\text{cpx/melt}}$) of the nearest neighbor calculation chain. Bédard (2014) notes that $D_{\text{REE}}^{\text{cpx/melt}}$ do not correlate well with melt or crystal-chemical properties that could be used to regress them from. Alternatively, Hack et al. (1994) proposed linking $D_{\text{REE}}^{\text{cpx/melt}}$ with $D_{\text{Ti}}^{\text{cpx/melt}}$. Bédard (2014) found a robust relation between these partition coefficients in the massive data set he compiled. The remaining problem is finding proper $D_{\text{Ti}}^{\text{cpx/melt}}$ values that are linked to measurable parameters with a reasonable correlation. Here we used the regression of $\text{Ln}D_{\text{Ti}}^{\text{cpx/melt}}$ versus Al^{IV} binned by melt SiO_2 . While Al^{IV} is calculated from EPMA data, some assumption has to be made regarding the melt SiO_2 for which two options are reasonable: either using SiO_2 source mass fraction as proposed by Kinzler and Grove (1993), which is 50.1 g/100 g SiO_2 or using the median bulk SiO_2 mass fraction from the Wadi Gideah gabbroic suite, $46.9 \pm 0.7 \text{ g/100 g SiO}_2$. We decided for the latter case, but it should be noted that both approaches lead to very similar results in our interpretation of the plagioclase clinopyroxene equilibrium, which is discussed below.

Assessing the similarity of calculated equilibrium melts for plagioclase and clinopyroxene and the comparison to the MORB compositional array of Oman basalts, it is possible to distinguish three characteristic cases for the 39 gabbros investigated here. (a) For the layered gabbros, equilibrium melt compositions for both phases show a good correspondence, implying that plagioclase and clinopyroxene cores crystallized under equilibrium boundary conditions (Figures 6g–6i). Both melts correspond well to the Oman MORB compositional array, implying that lower gabbros were formed as cumulates from those MORB parental melts which also fed the extrusive section; (b) Some equilibrium melts for both minerals from the foliated gabbros are

very similar, as for the layered gabbros, suggesting equilibrium crystallization conditions, but with respect to the MORB compositional array originate from a significantly enriched parental melt (Figures 6d–6f). This misfit indicates that these melts underwent a process of moderate to strong differentiation before crystallizing into foliated gabbro mineral cores. Consequently, they appear to have crystallized from MORB isolated liquids rather than forming from MORB as equilibrium cumulates. (c) Exceptions to this general picture where equilibrium melts for plagioclase and clinopyroxene show strongly contrasting compositions are found for two layered gabbros, some foliated gabbros, and the two varitextured gabbros (Figures 6a–6c and 7). For all the disequilibrium gabbros, the plagioclase equilibrium melt is: (a) systematically more enriched than the clinopyroxene equilibrium melt and (b) with respect to the Oman MORB array, more evolved than the upper compositional limit. Therefore, it is obvious that clinopyroxene saturation of parental melts for these samples was accomplished before plagioclase saturation. We identified two different reasons for this inconsistency: (a) all corresponding samples (Figure 7, pl-cpx ratio >1.5) are amphibole-bearing gabbros (incl. two hornblende gabbros) with high xAn plagioclase. Both indicate high water activity during crystallization, implying that the use of the applied distribution coefficients is inappropriate and the initial anorthite temperature is biased. (b) These samples show partially complex-zoned plagioclase, indicating a change in the boundary conditions during crystallization (i.e., the involvement of more differentiated melt composition and intense melt mixing during crystallization), driving the crystallizing phases into a state of disequilibrium. Nevertheless, to more comprehensively evaluate the scenario of melt mixing and differentiation under hydrous conditions on a geochemical basis, high precision full-grain compositional mappings of all phases along a consistent transect throughout the oceanic crust are needed for verification. This is beyond the scope of this study.

Another almost ubiquitous feature of the equilibrium melts with respect to the MORB compositional array is the increasing depletion of most incompatible elements, especially for plagioclase (e.g., Figures 6a, 6d, and 6g). Therefore, it is essential to consider whether this will affect the assessment of equilibrium and the subsequently derived $T_{\text{REE}}^{\text{pl/cpx}}$. Similar chemical characteristics are observed by Lissenberg et al. (2013, cf., their Figure 8a) for calculated plagioclase equilibrium melts from Hess Deep gabbros, except that plagioclase (and olivine) are more primitive than the EPR MORB compositional array, which is not the case for the Wadi Gideah gabbros. Lissenberg et al. (2013) argue that the D_{REE} would have to be changed by an unrealistic amount to fit the equilibrium melt of plagioclase (and olivine) to the MORB array. Thus the observed fractionation pattern represents a natural feature of the crystallizing system. In principle, we share their interpretation, but the cause for this cannot solely be explained by reactive porous flow, which causes a redistribution of incompatible elements from the gabbroic framework into the reactive porous melts, thus post-modifying the initially recorded mineral-melt equilibrium and inevitably leaving traces of this modification on the intergranular assemblage which is for Wadi Gideah lower gabbros absent in general. It is important to note that the compatibility-driven disequilibrium partitioning is not the same as a total disequilibrium between plagioclase and clinopyroxene since, on average, the REE parental melt ratio is still around 1 (i.e., Figures 6f and 6i). In contrast, at a total disequilibrium, it significantly diverges from 1 (i.e., Figure 6c). We suggest that the misfit of MORB and equilibrium melt signatures (i.e., the negative slope of plagioclase parental melt, Figures 6a, 6d, and 6g) primarily arises from delayed crystallization of plagioclase within hydrous melts, where clinopyroxene incorporates HREEs more efficiently than LREEs prior to plagioclase formation. In other words, the compatibility-driven disequilibrium partitioning leads to a plagioclase-clinopyroxene parental melt ratio superimposed by the compatibility-driven systematic misfit between MORB and plagioclase (i.e., negative slope, Figures 6c, 6f, and 6i). This interpretation is supported by the fact that plagioclase is significantly more affected by compatibility-driven disequilibrium partitioning than clinopyroxene (Figure 6). Although this circumstance does not preclude modification of trace element signatures by reactive porous flow within the lower crust, melt-rock interactions seem to play a minor role within Oman layered gabbros since significant zonation of incompatible trace elements is very limited and clinopyroxene equilibrium melt is not fractionated against MORB. Likely, the observed fractionation pattern will not survive the mixing of primitive melts into the AML since primitive melts delivered to the AML do not share the fractionated pattern observed for plagioclase (cf., Figure S3c in Supporting Information S1). Still, for the crust-internal development, this fractionation is essential since it is linked to the rotation of the $T_{\text{REE}}^{\text{pl/cpx}}$ regression, as discussed in the last paragraph of the next section.

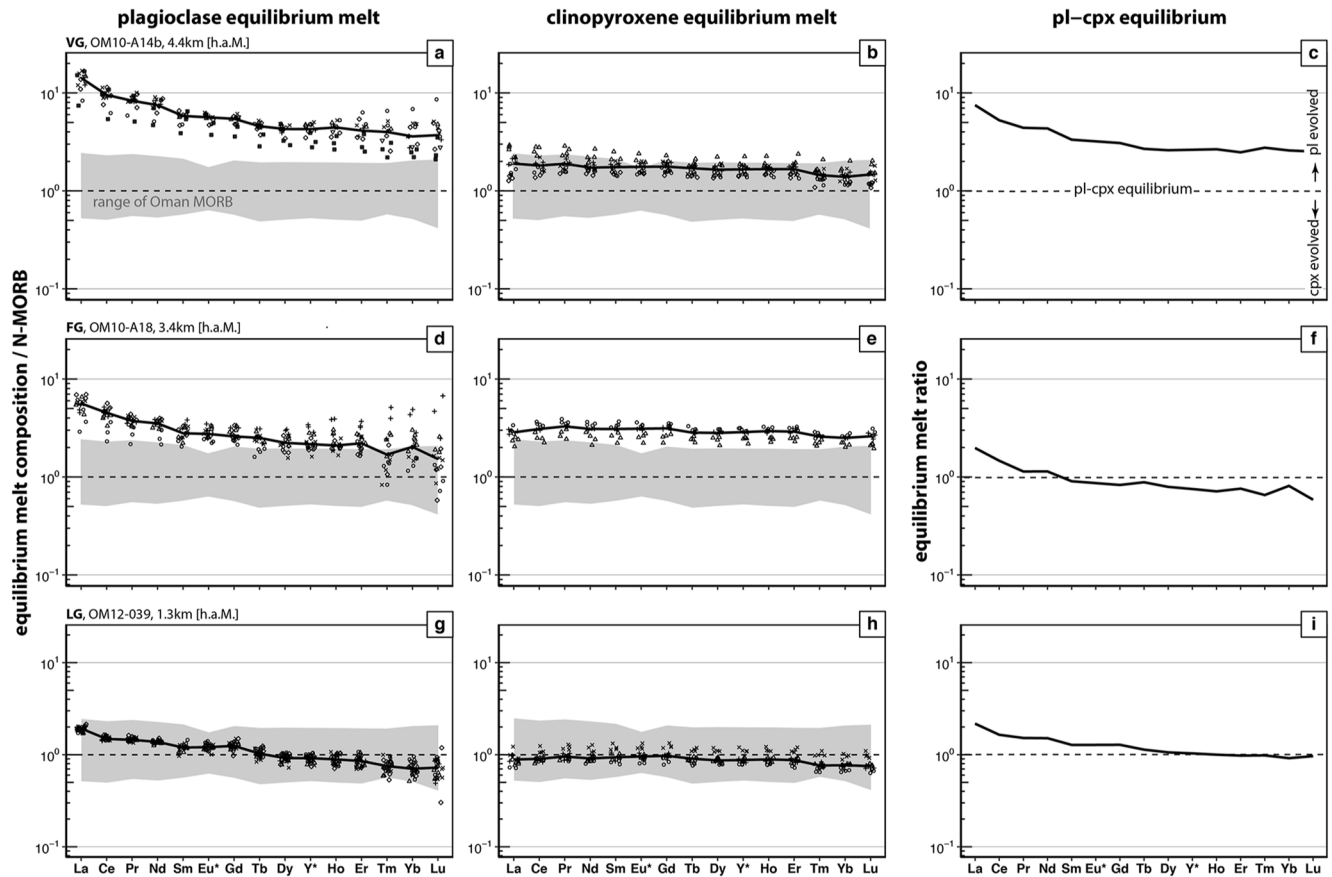


Figure 6. Equilibrium melt calculated from partitioning coefficients for plagioclase (a, d, and g) and clinopyroxene (b, e, and h) for core compositions of three representative samples of the main lithological units: layered gabbro (bottom), foliated gabbro (middle) and varitextured gabbro (top). The gray field corresponds to MORB compositions derived from sheeted dikes and pillow basalts from the Ibra area (Müller, 2015), normalized to N-MORB (Gale et al., 2013). (c, f, and i) Melt composition calculated for plagioclase divided by the one for clinopyroxene. Values around one imply equilibrium between plagioclase and clinopyroxene which is indicated for the layered and foliated gabbros but not for the varitextured gabbro.

4.4. Applicability and Reliability of the REE-In-Plagioclase-Clinopyroxene Thermometer

The REE exchange thermometer has recently been applied to gabbroic rocks by Sun and Lissenberg (2018), by Boulanger et al. (2020) and by Mock, Neave, et al. (2021). An option to verify the validity of temperatures is to couple the REE thermometer ($T_{\text{REE}}^{\text{pl/cpx}}$) to established anorthite thermometers (T_{An}). It is well known that the composition of plagioclase depends on crystallization temperature. A robust regression of temperatures for the 33 equilibrium samples (Figure 8a gray dots, disequilibrium samples: OM10-A13, OM12-A14b, OM15-27, OM10-A17, OM10-A20, and OM12-055 are excluded from regression), as derived from T_{REE} against anorthite-in-plagioclase reveals a relation of:

$$T_{\text{REE}}^{\text{An}} [^{\circ}\text{C}] = 6.1 \pm 0.2 * \text{An} + 706 \pm 19$$

The coupling of T_{An} to T_{REE} has recently been emphasized by Sun and Lissenberg (2018). They derive a slope for the anorthite-temperature regression ($T_{\text{S\&L18}}^{\text{An}}$) of $7.62^{\circ}\text{C} \times \text{An}^{-1}$, which is significantly higher than inferred from our regression and other An-thermometers (see below Figure 8). The reason for this lies in an erroneous averaging of the data by Sun and Lissenberg (2018), which have neither been checked for extreme values nor for equilibrium. Their data additional is not separated by core and rim compositions which inevitably leads to disequilibrium $D_{\text{REE}}^{\text{pl-cpx}}$ values. While the motivation to lump all data together lies in better representing the samples' average compositions, this approach is strictly invalid when using an equilibrium based thermometer as the one of Sun and Liang (2017). Additionally, for calculating T_{REE} , Sun and Lissenberg (2018) generally excluded the HREEs due to insufficient data quality or lack of plagioclase HREE data due to detection limit. As at least some of the Hess

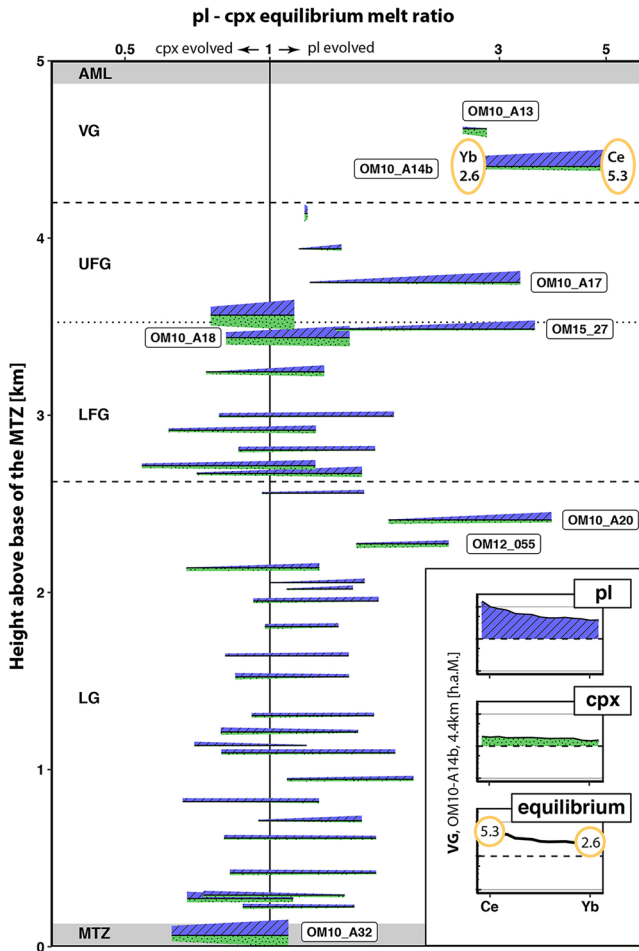


Figure 7. Equilibrium melt composition for $Ce_{p/Cpx}$ and $Yb_{p/Yb_{cpx}}$ based on mineral melt partitioning as described in Section 4.3, plotted against crustal depth. The x-axis represents the division of plagioclase equilibrium melt by clinopyroxene equilibrium melt (same as the y-axis in Figures 6c, 6f, and 6i). Therefore, a value around 1 implies equilibrium between plagioclase and clinopyroxene, which is indicated for most layered and foliated gabbros. The horizontal width of the lines represents the compatibility-driven deviation from absolute equilibrium for Ce & Yb (i.e., the distance to 1 as expressed in Figures 6c, 6f, and 6i) and therefore is equal to the REE slope as found in Figures 6c, 6f, and 6i. Colored areas (wedges) correspond to the absolute deviation between calculated equilibrium melts and the MORB composition (i.e., the distance to 1, which is N-MORB; Gale et al., 2013), as expressed in Figures 6a, 6b, 6d, 6e, 6g, and 6h. The top part (blue) corresponds to plagioclase, and the bottom part (green) to clinopyroxene. This deviation scales on the y-axis [km, h.a.M.] as $100 \times \log_{10}(REE/N-MORB)$, so it is basically a factor 100 scale of the y-axis of Figures 6a, 6b, 6d, 6e, 6g, and 6h. In other words, the wider the lines are, the stronger is the compatibility-driven disequilibrium between plagioclase and clinopyroxene (these samples rotate against the REE-thermometer). Moreover, the more the lines diverge from $x = 1$, the more the samples are out of general equilibrium, and the bigger the wedge is, the stronger is the disequilibrium between plagioclase and clinopyroxene equilibrium melts and the MORB melt. The inset to the bottom right represents a sketch of the first row of Figure 6 (Figures 6a–6c) and illustrates how this graph is created by taking sample OM10-A14b as an example (note the inverse and log scaled x-axis). For details and discussion, see text.

Deep samples are rotated within the thermometers $B/1000$ versus $Ln(D_j)-A$ space, this yields temperature estimates that are too high (see Section 2.3 and below), and puts their subsequent calculations in doubt. Several plagioclase-liquid equilibria thermometers are available (see data compilation and discussion in Putirka [2005, 2008]). Putirka (2008) shows that the precision of such thermometers gets worse as soon as water is involved in the crystallizing system. Therefore, he emphasizes the importance of estimating errors to make meaningful statements from calculated temperatures. Since in a gabbroic crustal system, the equilibrium melt is absent, a useful comparison can be made to well-studied mafic layered intrusions. VanTongeren and Mathez (2013) found a simple anorthite-in-plagioclase temperature relation based on observations made for the Bushveld complex by calculating liquidus temperatures using the plagioclase-liquidus equilibrium implemented in MELTS (Ghiorsio & Sack, 1995). In the temperature versus anorthite content regression, $T_{V\&M13}^{An}$, they found a slope of $6.8^\circ C \times An^{-1}$, very similar to the T_{REE}^{An} slope from our study. Temperature models derived from the Skaergaard layered intrusion linked to experiments performed by Thy et al. (2008, 2009), T_{Thy09}^{An} , reveal a much smaller slope of $3.6^\circ C \times An^{-1}$. The reason for this lies in the wrong coupling of equilibrium melting and fractional crystallization. Morse (2010) disproved their ruling hypothesis and recalculated the Skaergaard regression, $T_{Morse10}^{An}$, to a slope of $4.6^\circ C \times An^{-1}$. Feig et al. (2006) experimentally found very similar slopes (cf., their Figure 6). Additionally, their work suggests that the water content influences the regression parameters of anorthite against temperature, steepening the slope toward higher water contents. This is supported by crystallizing the Gideah Bulk crustal composition of Garbe-Schönberg et al. (2022) at different water contents using MELTS (Figure 8b). The model also suggests that the water content of the source melt was between 0.4 wt% H_2O and 0.6 wt% H_2O . For our initial guess of water content, we used 0.8 wt% H_2O following Müller et al. (2017) and MacLeod et al. (2013). Since the influence of water on $T_{REE}^{pl/cpx}$ is low (cf., Figure S2 in Supporting Information S1), it is insignificant for the thermal implication (Section 4.5) if a water content of 0.4 wt% H_2O or 0.8 wt% H_2O is used. Nevertheless, for the geochemical evolution of the Gideah oceanic crust it makes a notable difference as expressed by plagioclase evolution lines of fractional crystallization as a function of water content (Figure 8b). While any T_i^{An} model is in principle independent of the plagioclase-clinopyroxene equilibrium but highly susceptible to the prevailing water activity, the situation is opposite in terms of the $T_{REE}^{pl/cpx}$ model. Hence, if both thermometers reveal similar temperatures, the result can be assumed to be reliable.

Two varitextured gabbros (OM10-A13 and OM12-A14b), two foliated gabbros (OM15-27, OM10-A17), and two layered gabbros (OM10-A20 and OM12-055) show significant deviations from the robust T_{REE}^{An} regression (Figure 8a). These are exactly those samples, showing significant differences in the compositions of the calculated equilibrium melts (Figure 7). It is obvious that the disequilibrium leads to erroneous temperature estimates using the Sun and Liang (2017) thermometer. For all of these “disequilibrium gabbros,” calculated $T_{REE}^{pl/cpx}$ overestimate the true crystallization temperature substantially, so that they exceed the temperature range evaluated by the regression uncertainty (Figure 8a, gray dots). In principle, their offset can be corrected by projecting them onto the regression line of T_{REE}^{An} and adjusting the temperature accordingly (see Figures 8 and 10 and next section), but this still might lead to false temperature estimates. Given that for these samples, clinopyroxene is significantly more primitive than plagioclase and primary

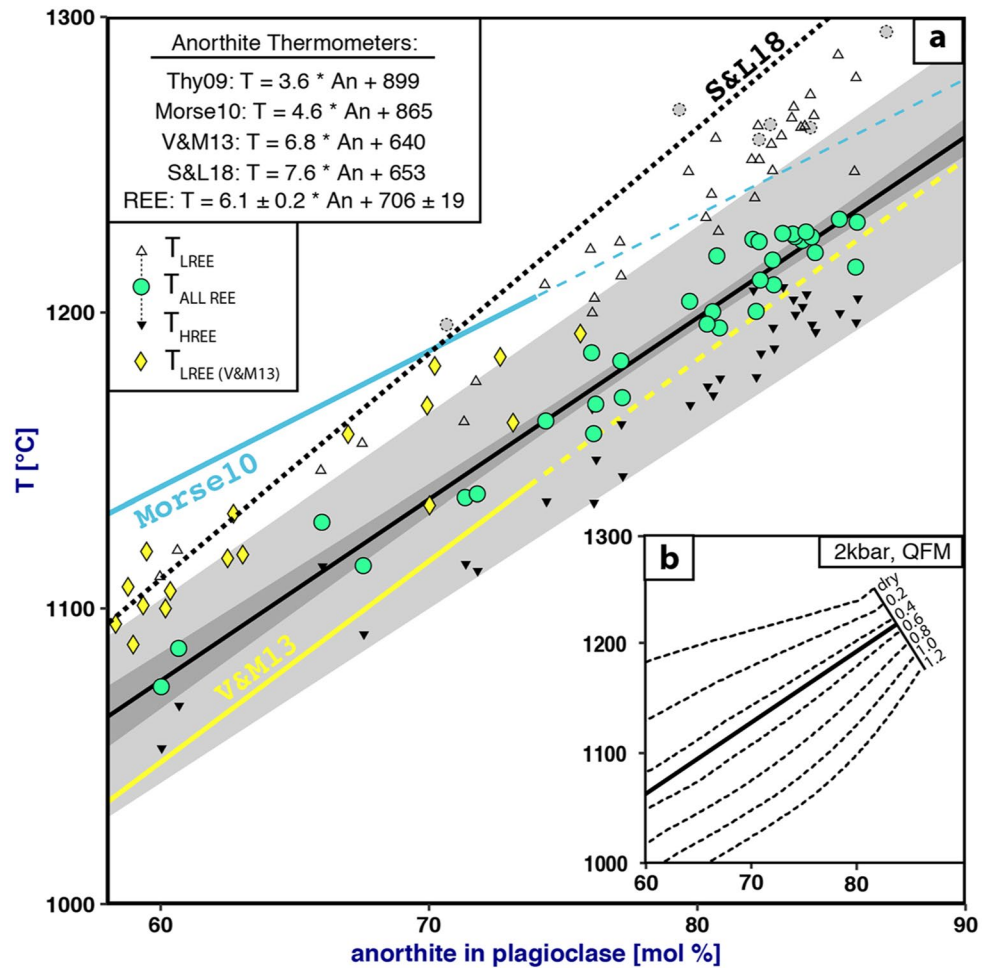


Figure 8. Relationship between anorthite content of plagioclase and temperature. (a) Calculated REE-equilibrium temperature as a function of anorthite in plagioclase. Shown are the functions of three geo-thermometers based on the anorthite content in plagioclase S&L18 (Sun & Lissenberg, 2018), Morse10 (Morse, 2010), and V&M13 (VanTongeren & Mathez, 2013). Green dots represent the 33 samples of this study which are in equilibrium, yielding valid temperatures, calculated using the $T_{\text{REE}}^{\text{pl/cpx}}$ thermometer of Sun and Liang (2017). The robust regression at a confidence interval of 95% (dark gray area) of this relation gives the $T_{\text{REE}}^{\text{An}}$ thermometer (black line) and the related error region (light gray area). The six disequilibrium samples (gray dots) are falling off the plausible $T_{\text{REE}}^{\text{An}}$ range (see also Figures 7 and 10 and text). These samples are excluded from $T_{\text{REE}}^{\text{An}}$ regression. For each sample, temperatures for HREEs (closed triangles) and LREEs (open triangles) have been calculated separately to illustrate the severe effect of REE-group exclusion during $T_{\text{REE}}^{\text{pl/cpx}}$ regression if rotation is present in the REE data (see also Figure S7 in Supporting Information S1 and text for details). Yellow diamonds represent REE-temperatures of the V&M13 data. As this data set lacks HREE compositions for plagioclase and rotation is present, the resulting temperatures are about 50°C too high, showing that HREE/LREE temperature offsets are not a unique feature of Wadi Gideah gabbros. (b) Plagioclase fractional crystallization evolution lines for different water contents (dashed lines) of the Gideah Bulk Crust composition (Garbe-Schönberg et al., 2022) modeled with MELTS at 2 kbar buffered by QFM (Ghiorso & Sack, 1995). The main result here is that the anorthite-temperature trend of the Wadi Gideah gabbros (solid black line, equal to Figure 8a) can only be explained for a water content between 0.4 and 0.6 wt% H_2O . For details see discussion.

interstitial amphiboles and an enhanced overgrowth of clinopyroxene by hornblende is omnipresent, the water content of their parental melt likely exceeded 3 wt% H_2O elevating their xAn content. The influence of water on the anorthite temperature becomes more significant as water content increases ($\Delta \text{xAn} \sim 10\text{An/wt\% H}_2\text{O}$ @ 1100°C & 2kbar, Feig et al., 2006), lowering the true crystallization temperature of samples crystallized from wet magma. In other words, temperatures calculated by any An-in-plagioclase-thermometer will increasingly overestimate the true crystallization temperature with increasing water content of the parental melt. Possibly neither $T_{\text{REE}}^{\text{pl/cpx}}$ nor $T_{\text{REE}}^{\text{An}}$ yield reliable results for the disequilibrium samples and, therefore, they should be treated with

caution. Still, if $T_{\text{REE}}^{\text{pl/cpx}}$ matches $T_{\text{REE}}^{\text{An}}$ and plagioclase-clinopyroxene equilibrium is given, the calculated temperatures are trustworthy if $T_{\text{REE}}^{\text{pl/cpx}}$ is calculated from all REEs.

For all gabbro samples, the temperature inversion (forced through the origin of B_j-1000 and $\ln(D_j)-A$) is rotated against the rare earth elements systematically by their periodic number, with LREE below the regression and HREEs above (cf., Figure 2, Figure S1 in Supporting Information S1). To a limited extent, such rotation can be caused by the evolution of the parental magma, as shown for a modeled evolving composition by Sun and Liang (2017, cf., their Figure S2). We found a coarse correlation (Figures S5 and S6 in Supporting Information S1) between the rotation, expressed as an offset from the origin (regression over REEs not forced through origin) and the REE slope of plagioclase-clinopyroxene equilibrium melts, as shown in Figures 6c, 6f, and 6i (see also Figure S3c in Supporting Information S1). Obviously, the REE fractionation between plagioclase and clinopyroxene in the calibration data of Sun and Liang (2017) is different compared to the Oman Wadi Gideah gabbros. This behavior is also seen for many other natural gabbroic samples (see data compiled by Sun and Liang [2017]) and for some of the Hess Deep gabbros (Sun & Lissenberg, 2018). The consequence of the rotation is that temperatures exclusively calculated from LREE are always higher than those calculated from HREE (Figure 8a). This is obvious because both parameters B_j-1000 and $\ln(D_j)-A$ are negative (regression within the third quadrant of the coordinate system), and rotation regression always has a lower slope than temperature regression. If only LREEs are regressed for temperature, rotation is lower, and therefore compensation for rotation is weaker and vice versa for HREEs. In other words, if only LREEs are accounted for, true rotation is underestimated, and the temperature regression gets pulled toward the LREEs, resulting in an erroneous high temperature regression slope and temperature estimate. Since this effect can introduce a temperature uncertainty of up to 90°C, it is the most severe source of error when applying the plagioclase-clinopyroxene equilibrium thermometer (given that plagioclase and clinopyroxene are in equilibrium). As higher the rotation as more severe this effect is (see the correlation in Figure S7 of Supporting Information S1), and as more important it is to include all REEs into the temperature calculation to compensate for rotation accurately. An example that shows the above mentioned is expressed by calculating $T_{\text{REE}}^{\text{pl/cpx}}$ for the VanTongeren and Mathez (2013) data. While their $T_{\text{V\&M13}}^{\text{An}}$ regression is trustworthy as it is based on MELTS equilibrium calculations, the REE-temperatures calculated from their data are ~50°C too high due to the lack of HREE data (Figure 8a). Another example is the erroneous $T_{\text{S\&L18}}^{\text{An}}$ regression which is in the range of $T_{\text{REE}}^{\text{pl/cpx}}$ being calculated from only LREEs (open triangles and diamonds, Figure 8a) or disequilibrium samples (gray dots, Figure 8a), or to the worse, both. It has to be noted that the rotation effect is more substantial if HREEs are excluded because HREEs for many samples not only diverge from temperature regression but also from rotation regression more severely than LREEs (cf., Figure S1 in Supporting Information S1, HREE divergence from dashed lines). One reason for this might be that $T_{\text{REE}}^{\text{pl/cpx}}$ is solidly calibrated mainly against LREEs because published data for plagioclase-melt compositions for HREEs are rare, which is a consequence of their low mass fraction in plagioclase, which is close to the detection limit and their large associated uncertainties. Conclusively, it has to be noted that if REE rotation is present in a data set, the exclusion of certain REEs (especially a whole group, e.g., HREEs) for a subset of samples will lead to inconsistencies in the resulting temperature data set and to wrong temperature estimates for these samples. Hence, we included all REEs for all samples in the calculation.

4.5. Geochemical Implications and Thermal Structure of the Wadi Gideah Oceanic Crust

The Oman ophiolite crust's overall evolutionary trend, as recorded in the gabbros (Figure 9a), follows fractional crystallization much better than the Hess Deep gabbros do (Coogan, Gillis, et al., 2002). Nevertheless, a widely recognized over-enrichment of incompatible elements (cf., Figure 1a in Coogan and O'Hara [2015]) is also present in the Wadi Gideah Transect gabbros (Figure 9b), especially in the upper gabbros and rims of some lower gabbros. These trends are not explained by conventional closed system crystallization mechanisms but possibly reflect more complex open system processes (e.g., RMTX magma chambers, Coogan & O'Hara, 2015, and reference therein). For Wadi Gideah, strong indications for crust internal melt evolution (cf., Figures 3 and 4) are: (a) the progressive shift of differentiation indices toward higher degrees of fractionation, increasing from MTZ to AML (Mg#, TiO₂, and Cr in cpx) and (b) a more or less consistent enrichment of incompatible trace elements (Ba, REEs in pl; REEs in cpx) in mineral cores. Mass fractions of Zr correlates negatively with a decrease of Eu/Eu* in clinopyroxene (Figure 9c). This relation indicates trace element enrichment during clinopyroxene evolution accompanied by a reduction in melt mass due to plagioclase crystallization (Lissenberg et al., 2013).

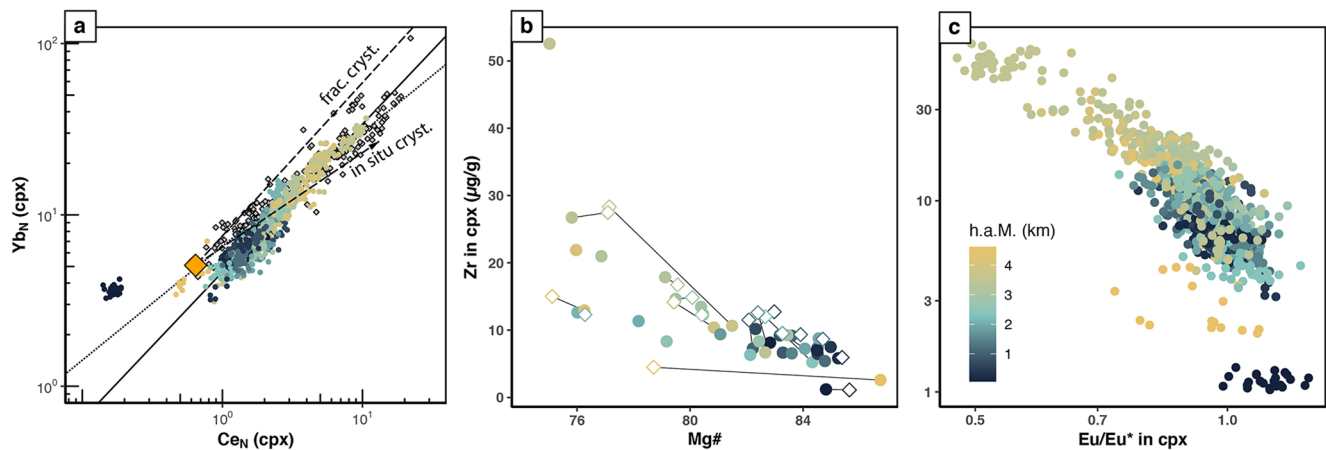


Figure 9. Geochemical indices for clinopyroxene of the Wadi Gideah crustal transect. (a) Trace element fractionation trend expressed as Yb_N over Ce_N for Wadi Gideah gabbros (solid black line, circles, colored according to h.a.M., see legend), compared to gabbros from Hess Deep (dotted black line, gray diamonds). For comparison, the fractionation model of Coogan, Gillis, et al. (2002) is plotted (long dashed lines, large orange diamond is Hess Deep source composition, for details see Figure 6 in Coogan, Gillis, et al. [2002]). The Wadi Gideah trend follows fractional crystallization much better than Hess Deep gabbros, but has a different source composition with less Yb and more Ce. (b) Zr in clinopyroxene as a function of Mg# (dots represent the core composition, open diamonds are for rim composition). Lines connect the individual core-rim pairs. (c) Zr over Eu/Eu^* indicates a decrease in melt mass during clinopyroxene fractionation due to plagioclase crystallization. For details, see text.

Incompatible trace element ratios (e.g., $(La/Sm)_N$ in plagioclase and Zr/Hf in clinopyroxene) are near-constant within the layered gabbros but become more variable and higher in the foliated gabbros (cf., Figures 3f and 3m). Hence, the upper part of the crust, if compared to the lower crust, crystallized from more evolved melts and was influenced by changing boundary conditions, while the lower part of the crust represents a near steady-state crystallization system.

The thermal structure of the crust expressed as density distributions as a function of distance to the MTZ (Figure 10) strongly supports the above discussed observations. The crystallization temperature of the crystal mush framework that formed the layered gabbros falls in a narrow range of about $1216 \pm 14^\circ\text{C}$ (Figure 10, up to a crustal height of 2 km H.a.M., ignoring sample OM10-A32 from the MTZ). On the contrary, large variability of temperature ranging from 1077 to 1231°C can be observed further up section. The lower crustal temperature correlates very well with MELTS-modeled crystallization temperatures for magma expelled from the mantle and fed into the crust crystallizing in situ (Figure 10, Kelemen & Aharonov, 1998). Crystallization rates depend on the style of crystallization and composition of the initial liquid; in any case, they are relatively high ($>1\% \text{ } ^\circ\text{C}^{-1}$) as soon as plagioclase saturation is reached. Consequently, a large amount of melt will crystallize if the temperature is reduced by only some 10°C below the plagioclase liquidus (Kelemen & Aharonov, 1998). Although enhanced water content of the parental melt will lower the plagioclase saturation temperature, the presence of a widely molten magma chamber within the lower crust is not observed by crustal tomography (e.g., Dunn et al., 2000) or compliance modeling (e.g., Crawford & Webb, 2002; Zha et al., 2014). Therefore, melt intruding the lower crust either has to move rapidly toward the AML before becoming saturated in plagioclase, or it will start to crystallize and generate latent heat that has to be removed efficiently to avoid forming a molten lower crustal magma reservoir. Field, petrographic and geochemical evidence for the existence of a high-temperature hydrothermal system active in the lower crust is numerous (e.g., Bosch et al., 2004; Currin et al., 2018; Dygert et al., 2017; Koepke et al., 2005a, 2005b; Koepke, Mueller, et al., 2014; Nicolas & Mainprice, 2005; Wolff et al., 2013; Zihlmann et al., 2018). This system is likely to be channelized, following either a microcrack system (Nicolas & Mainprice, 2005) or hydrothermal fault zones (Coogan et al., 2006; Zihlmann et al., 2018). Therefore, latent heat consumption by hydrothermal cooling varies dramatically with distance to the fluid flow channels. This heterogeneous permeability structure of the crust gives a plausible reason that along one-dimensional crustal profiles, very contrasting cooling rates are found for Hess Deep and Oman (e.g., Coogan, Jenkin, & Wilson, 2002; Faak & Gillis, 2016; Faak et al., 2015; VanTongeren et al., 2008), and also explains why coupled models of magmatic accretion and hydrothermal flow (Theissen-Krah et al., 2011, 2016) fail to generate the crust with less than 50% “glacier” mush flow without introducing a largely molten magma reservoir in the lower crust. Hasenclever

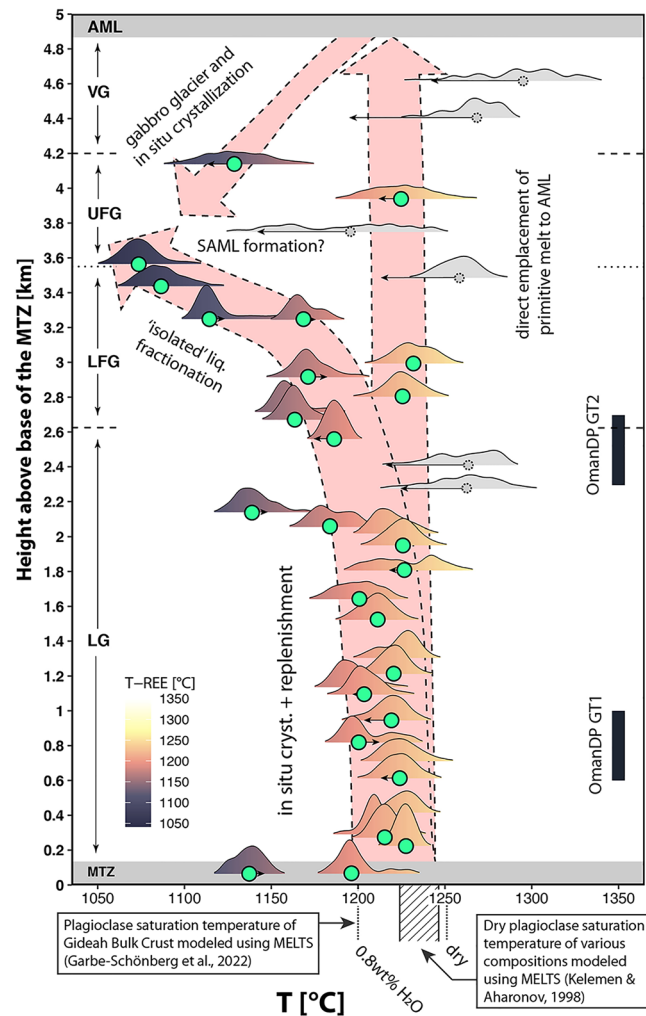


Figure 10. Crystallization temperature density distribution as a function of crustal depth (shaded by temperature, see legend). The density range represents temperature distributions based on outer matrix $D_{REE}^{pl/cpx}$ calculations for all spots analyzed within a given sample (for details, see text). Median values are marked with green dots. Arrows originating at the dots show the distribution shift necessary to equalize between the REE-temperature and the An-temperature (so that the tips of the arrows represent the corresponding An-temperature) based on the $T_{REE}^{pl/cpx} - T_{REE}^{An}$ relation (Figure 8a). Most of the layered gabbros have crystallized in a narrow temperature range averaging around 1216°C. The foliated gabbros show a more extensive temperature range and broader distributions for many samples. One branch (light red arrow) leads to crystallization temperatures that reflect lower liquidus temperatures (around 1077°C), and another branch shows temperatures similar to the layered gabbro range. Those samples with the highest temperatures together with the two varitextured gabbros are subjected to significant disequilibrium between plagioclase and clinopyroxene, their temperatures are not reliable (shaded gray, also see Figures 7 and 8a and discussion on disequilibrium gabbros). The black columns labeled GT1 and GT2 represent drill cores of the OmanDP (Kelemen et al., 2020a, 2020b). The thermal minimum likely reflects a zone where SAMLs fed from the top and bottom can form. At the bottom of the graph, two temperature ranges for plagioclase saturation are indicated as derived from MELTS. The hatched area represents dry plagioclase saturation for different parental melt compositions (for details, see Kelemen & Aharonov, 1998). The area confined by the dashed lines represents the plagioclase saturation temperatures for the Gideah Bulk Crust composition for different water contents (see Figure 8b and text for details). For calculation and details, see text and methods sections and Sun and Liang (2017) for fundamentals on the temperature inversion.

et al. (2014) demonstrate numerically that a relatively uniform heat removal within the lower crust could be achieved by off-axis recharge, deep hydrothermal circulation discharging into the shallow on-axis circulation system. Still, somewhat crude assumptions have to be made concerning the permeability since neither the total permeability, the anisotropy of permeability, nor the geometric permeability structure is known in sufficient detail.

A remarkable feature of the thermal structure is a thermal minimum within the middle part of the foliated gabbros near 3.5 km height above MTZ. MacLennan et al. (2004, 2005) present a numerical thermal model of the lower oceanic crust, showing that the thermal structure is a result of the accretion mechanism. For a hybrid scenario where the upper crust forms by a crystal mush “glacier” originating from the AML and the lower crust forms in situ, the model develops a temperature minimum between these two regimes, which mirrors the $T_{\text{REE}}^{\text{pl/cpx}}$ in situ thermal structure very well. The variable temperature record and geochemical complexity of the foliated gabbros are likely to be caused by the mixing of melts that have undergone very different flow and fractionation patterns. Recent geophysical studies suggest that multiple small melt lenses carrying a higher melt fraction than formerly thought are present in the upper oceanic crust at the on-axis (Carbotte et al., 2021; Marjanović et al., 2014) and off-axis region (Han et al., 2014). These sub axial on-axis melt lenses (SAML) have been observed down to a depth of up to 1.6 km below the AML, coinciding with the thermal minimum outlined above. These melts are possibly diverse in composition, given the wide compositional range found for the upper foliated gabbros. It is commonly agreed that the steep foliation pattern of the foliated gabbros is a consequence of the mush flow direction, which is for the upper crust dominantly sub-vertical (e.g., MacLeod & Yaouancq, 2000; Nicolas et al., 2009, and reference therein). The rapid increase of strain measured for plagioclase directly below the AML (Nicolas et al., 2009) is caused by the rotation of plagioclase toward the steeply dipping foliation. It is only preserved in the rock if mush flow characteristics change from suspension to rigid flow at the time of plagioclase rotation. The increase in fractionation and the low temperatures recorded toward a crustal level of 3.5 km h.a.M., suggests that SAMLs are fed from both the top and the bottom (Figure 10, Boudier et al., 1996). On the one hand, divergent plates cause a downward suction (Nicolas et al., 2009) of crystal/melt mixtures present at the bottom of the AML to feed the SAMLs from the top. The steep foliation found in the gabbros below the AML, a structure present throughout the ophiolite and outlined by Quick and Denlinger (1993), modeled by Chenevez et al. (1998), and described in detail by Nicolas et al. (2009), is one of the primary petrological indications for “glacier-like” flow dynamics. Still, MacLeod and Yaouancq (2000) suggest that the foliation can also be a consequence of enhanced upward flow, likely both is possible. On the other hand, melts expelled from the lower gabbro cumulus can also be fed into SAML reservoirs from below. As our data suggest by the fractionation characteristics of rim compositions of samples within the lower crust, such melts feature an increased water content and a moderately evolved geochemical signature. Mixing these melts with melts and mushes subsiding from the AML leads to the complex evolution of the foliated gabbros, which is also evidenced by the increase in zonation intensity toward a crustal level of 3.5 km h.a.M. Lastly, the AML is not present at a constant depth in the crust, but the largely molten reservoir is subjected to vertical shifts and downward extension into the foliated gabbros, possibly explaining the presence of frozen axial magma chambers within the foliated gabbros (France et al., 2009).

The significant temperature difference found for the layered and the series of foliated gabbros contradicts a gabbro glacier formation mechanism extending down to the MTZ. It is implausible that neither the diverse chemical composition nor the low temperature record of the upper crust can be found within the lower crust, if a full-depth crustal gabbro glacier would exist. These signatures would inevitably be transported to the lower crust by the vertical flow dynamics of a glacier. Here we show that both the calculated temperatures and the nature of the crystallization process (equilibrium vs. disequilibrium) are different for the lower and upper crustal levels. In situ crustal formation within a replenished-tapped magma chamber (Coogan & O'Hara, 2015) is much more likely to cause the Oman geochemical trends, since such magma chambers can buffer the major element evolution while enriching trace elements, including H_2O , at the same time, allowing for inverse zonation of plagioclase while fractionating trace elements upsection.

5. Conclusions

We have studied and analyzed 39 samples of the Wadi Gideah crustal transect in Oman to evaluate the primary processes of crustal formation as a function of crustal depth. We used major and trace element compositions of plagioclase and clinopyroxene of the gabbros, focusing on the core compositions. We show that the REE-in-plagioclase-clinopyroxene thermometer represents a robust tool to reveal insights on the de facto thermal structure of fast-spread oceanic crust.

Within the lower crustal interval (layered gabbros), Mg# and Ca# in clinopyroxene and plagioclase cores are nearly constant. REEs and other incompatible trace elements increase systematically from MTZ upwards to

the foliated gabbros. Calculated crystallization temperatures based on the REE-in-plagioclase-clinopyroxene thermometer yield a homogeneous temperature structure of $1216 \pm 14^\circ\text{C}$ for the lower crust. Crystallization proceeded under equilibrium, near steady-state conditions as indicated by the similarity in composition of the calculated equilibrium melts for plagioclase and clinopyroxene. Their similarity to the Oman MORB compositional array shows that layered gabbros are equilibrium cumulates of MORB parental melts. The depth coupled development of geochemical indices within a nearly invariant temperature regime gives evidence for crust internal evolution, with major elements being buffered by replenishment while incompatible elements are enriched by differentiation. These findings can only be explained by in situ formation of the lower crust.

For the layered gabbros, most plagioclase rims are moderately but significantly inverse zoned in Ca#, caused by an increase in water activity during rim crystallization. The increasing water content is likely a result of in situ fractionation within a hydrous parental melt with an initial water content between 0.4 and 0.6 wt% H_2O . Nevertheless, the influence of near axis high-temperature hydrothermal systems cannot be excluded and needs further attention.

Highly evolved compositions first occur within the uppermost layered gabbros, and the degree of fractionation increases to a maximum within the middle foliated gabbros, which are characterized by highly variable compositions and a wide range of crystallization temperatures ranging from 1077 to 1231°C . Generally, they feature elevated $(\text{La}/\text{Sm})_N$ and Zr/Hf ratios in plagioclase and clinopyroxene, respectively, with a sharp transition in incompatible element mass fraction and ratios of incompatible elements to the subjacent crust. Disequilibrium is mainly introduced by more primitive clinopyroxene, resulting from enhanced water content and delayed, hence evolved plagioclase crystallization. Some foliated gabbros contain high modal amounts of primary amphiboles, showing that trapped, isolated, and evolved batches of melt are present in the upper crust. Therefore, foliated gabbros partially represent frozen liquids instead of pure cumulate rocks.

Both foliated and varitextured gabbros display a high compositional variability in plagioclase and clinopyroxene core compositions for both major and trace elements, indicating dynamic processes present at the crystal grain scale. This complex compositional pattern is neither a product of mixing nor hydrous differentiation alone. It can be best explained by open system differentiation of melts and mushes that subside from the AML and mix with melts expelled from the lower crust to form sub-axial magma lenses (SAML), as recently discovered by seismic experiments. To resolve these dynamics, comprehensive chemical mappings of thin section assemblages along a consistent transect through the upper crust are needed. This study does not cover them but provides the basis for future studies on fine-scaled accretion dynamics of the ocean crust.

The most primitive composition of the whole crustal profile is found in cores of plagioclase and clinopyroxene of a varitextured gabbro, yielding LREE depleted signatures likely influenced by ultra depleted melt (UDM) compositions. These melts are more primitive than the most primitive Oman MORB and possibly never erupt prior to mixing with evolved melts in the AML eruptive reservoir. Such primitive melts must be widely isolated from the lower crust internal differentiation processes in order to maintain their compositional characteristics while rising through the magmatic plumbing system.

In summary, our results cannot be explained solely by the gabbro glacier or sill injection models but require a hybrid model. Although our data are consistent with the gabbro glacier process taking place in the upper portion of the lower crust (varitextured and upper foliated gabbros), they indicate that in situ crystallization forms the lower crust. Assuming a full crustal gabbro glacier, the complex signatures found within the upper crust would inevitably be transported to lower regions. Instead, the lowermost crust is widely homogeneous in its primary signature and temperature record. Therefore, our study emphasizes the importance of a deep hydrothermal cooling system that needs to be explored and characterized in more detail to allow for high-resolution coupled modeling of the interaction between the magmatic and hydrothermal regimes.

Data Availability Statement

Data produced for this work and discussed within this paper is available on the FAIR-aligned Pangaea repository (Müller et al., 2021; <https://doi.org/10.1594/PANGAEA.934706>). The R script for plagioclase-clinopyroxene-REE temperature calculation is available at GitHub and Zenodo (Müller, 2021; <https://doi.org/10.5281/zenodo.5702687>).

Acknowledgments

The authors highly appreciate the support of the Oman Public Authority For Mining for permission to conduct fieldwork in Oman. Special thanks go to Dr. Ali Al Rajhi, Dr. Mohamed Al Batashi, and Dr. Mohamed Al Arami. The authors kindly thank Prof. Dr. Sobhi Nasir from the geological department of the Sultan Qaboos University for assistance in planning and conducting fieldwork and shipping samples. The authors are thankful for detailed reviews by Michael Perfit and an anonymous colleague. Comments and thoughts by John Lassiter significantly advanced the manuscript—thank you very much. The authors acknowledge the work of the Hanover preparation lab for producing excellent thin sections. Special thanks go to Ulrike Westernströer and the Kiel University ICP-MS Lab team for their great support in conducting LA-ICP-MS analysis. The authors also thank the Kiel University and Hannover University EPMA lab teams for support with micro-analysis. This work was funded by the Deutsche Forschungsgemeinschaft (DFG, German Research Foundation) by a grant given to Dr. Dieter Garbe-Schönberg and Prof. Dr. Jürgen Koepke, project no.: 214851514. Open access funding enabled and organized by Projekt DEAL.

References

- Abily, B., & Ceuleneer, G. (2013). The dunitic mantle-crust transition zone in the Oman ophiolite: Residue of melt-rock interaction, cumulates from high-MgO melts, or both? *Geology*, 41(1), 67–70. <https://doi.org/10.1130/G33351.1>
- Abily, B., Ceuleneer, G., & Launeau, P. (2011). Synmagmatic normal faulting in the lower oceanic crust: Evidence from the Oman ophiolite. *Geology*, 39(4), 391–394. <https://doi.org/10.1130/G31652.1>
- Aghaei, O., Nedimović, M. R., Carton, H., Carbotte, S. M., Canales, J. P., & Mutter, J. C. (2014). Crustal thickness and Moho character of the fast-spreading East Pacific Rise from 9°42'N to 9°57'N from poststack-migrated 3-D MCS data. *Geochemistry, Geophysics, Geosystems*, 15(3), 634–657. <https://doi.org/10.1002/2013GC005069>
- Babcock, J. M., Harding, A. J., Kent, G. M., & Orcutt, J. A. (1998). An examination of along-axis variation of magma chamber width and crustal structure on the East Pacific Rise between 13°30'N and 12°20'N. *Journal of Geophysical Research*, 103(B12), 30451–30467. <https://doi.org/10.1029/98JB01979>
- Bédard, J. H. (2006). Trace element partitioning in plagioclase feldspar. *Geochimica et Cosmochimica Acta*, 70(14), 3717–3742. <https://doi.org/10.1016/j.gca.2006.05.003>
- Bédard, J. H. (2014). Parameterizations of calcic clinopyroxene—Melt trace element partition coefficients. *Geochemistry, Geophysics, Geosystems*, 15(2), 303–336. <https://doi.org/10.1002/2013GC005112>
- Berndt, J. (2002). *Differentiation of MOR Basalt at 200 MPa: Experimental Techniques and Influence of H₂O and fO₂ on phase Relations and liquid Line of descent* (Doctoral dissertation). Hannover Universität. <https://doi.org/10.15488/5960>
- Bieseler, B., Diehl, A., Jöns, N., Lucassen, F., & Bach, W. (2018). Constraints on cooling of the lower ocean crust from epidote veins in the Wadi Gideah section, Oman ophiolite. *Geochemistry, Geophysics, Geosystems*, 19(11), 4195–4217. <https://doi.org/10.1029/2018GC007679>
- Bosch, D., Jamaïs, M., Boudier, F., Nicolas, A., Dautria, J.-M., & Agrinier, P. (2004). Deep and high-temperature hydrothermal circulation in the Oman ophiolite—Petrological and isotopic evidence. *Journal of Petrology*, 45(6), 1181–1208. <https://doi.org/10.1093/petrology/egh010>
- Boudier, F., & Nicolas, A. (2011). Axial melt lenses at oceanic ridges — A case study in the Oman ophiolite. *Earth and Planetary Science Letters*, 304(3), 313–325. <https://doi.org/10.1016/j.epsl.2011.01.029>
- Boudier, F., Nicolas, A., & Ildefonse, B. (1996). Magma chambers in the Oman ophiolite: Fed from the top and the bottom. *Earth and Planetary Science Letters*, 144(1), 239–250. [https://doi.org/10.1016/0012-821x\(96\)00167-7](https://doi.org/10.1016/0012-821x(96)00167-7)
- Boudier, F., Nicolas, A., Ildefonse, B., & Jousset, D. (1997). EPR microplates, a model for the Oman ophiolite. *Terra Nova*, 9(2), 79–82. <https://doi.org/10.1111/j.1365-3121.1997.tb00007.x>
- Boullanger, M., France, L., Deans, J., Ferrando, C., Lissenberg, J., & von der Handt, A. (2020). Magma reservoir formation and evolution at a slow-spreading center (Atlantis Bank, Southwest Indian Ridge). *Frontiers in Earth Science*, 8, 397. <https://doi.org/10.3389/feart.2020.554598>
- Brice, J. C. (1975). Some thermodynamic aspects of the growth of strained crystals. *Journal of Crystal Growth*, 28(2), 249–253. [https://doi.org/10.1016/0022-0248\(75\)90241-9](https://doi.org/10.1016/0022-0248(75)90241-9)
- Browning, P. (1982). *The petrology, geochemistry and structure of the plutonic rocks of the Oman ophiolite* (Doctoral dissertation). The Open University. <https://doi.org/10.21954/ou.ro.0000de14>
- Buck, W. R. (2000). Can downward flow of dense cumulate slurry through mushy upper gabbros produce lower gabbros at a fast-spreading center? In Y. Dilek, E. M. Moores, D. Elthon, & A. Nicolas (Eds.), *Ophiolites and oceanic crust: New insights from field studies and the ocean drilling program. GSA Special Papers* (Vol. 349, pp. 0–127). Geological Society of America. <https://doi.org/10.1130/0-8137-2349-3.121>
- Carbotte, S. M., Marjanović, M., Arnulf, A. F., Nedimović, M. R., Canales, J. P., & Arnoux, G. M. (2021). Stacked magma lenses beneath mid-ocean ridges: Insights from new seismic observations and synthesis with prior geophysical and geologic findings. *Journal of Geophysical Research: Solid Earth*, 126(4), 1–19. <https://doi.org/10.1029/2020JB021434>
- Carbotte, S. M., Marjanović, M., Carton, H., Mutter, J. C., Canales, J. P., Nedimović, M. R., et al. (2013). Fine-scale segmentation of the crustal magma reservoir beneath the East Pacific Rise. *Nature Geoscience*, 6(10), 866–870. <https://doi.org/10.1038/ngeo1933>
- Carbotte, S. M., Smith, D. K., Cannat, M., & Klein, E. M. (2016). Tectonic and magmatic segmentation of the global ocean ridge system: A synthesis of observations. *Geological Society, London, Special Publications*, 420(1), 249–295. <https://doi.org/10.1144/SP420.5>
- Chenevez, J., Machetel, P., & Nicolas, A. (1998). Numerical models of magma chambers in the Oman ophiolite. *Journal of Geophysical Research*, 103(B7), 15443–15455. <https://doi.org/10.1029/98JB00597>
- Cherkaoui, A. S. M., Wilcock, W. S. D., Dunn, R. A., & Toomey, D. R. (2003). A numerical model of hydrothermal cooling and crustal accretion at a fast spreading mid-ocean ridge. *Geochemistry, Geophysics, Geosystems*, 4(9). <https://doi.org/10.1029/2001GC000215>
- Coleman, R. G. (1977). *Ophiolites*. Springer. <https://doi.org/10.1007/978-3-642-66673-5>
- Coleman, R. G. (1981). Tectonic setting for ophiolite obduction in Oman. *Journal of Geophysical Research*, 86(B4), 2497–2508. <https://doi.org/10.1029/JB086iB04p02497>
- Coogan, L. A. (2014). 4.14 – The Lower Oceanic crust. In H. D. Holland & K. K. Turekian (Eds.), *Treatise on geochemistry* (2nd ed., pp. 497–541). Elsevier. <https://doi.org/10.1016/B978-0-08-095975-7.00316-8>
- Coogan, L. A., & Dosso, S. E. (2016). Quantifying parental MORB trace element compositions from the eruptive products of realistic magma chambers: Parental EPR MORB are depleted. *Journal of Petrology*, 57(11–12), 2105–2126. <https://doi.org/10.1093/petrology/egw059>
- Coogan, L. A., Gillis, K. M., MacLeod, C. J., Thompson, G. M., & Hékinian, R. (2002). Petrology and geochemistry of the lower ocean crust formed at the East Pacific Rise and exposed at Hess Deep: A synthesis and new results. *Geochemistry, Geophysics, Geosystems*, 3(11), 1–30. <https://doi.org/10.1029/2001GC000230>
- Coogan, L. A., Howard, K. A., Gillis, K. M., Bickle, M. J., Chapman, H., Boyce, A. J., et al. (2006). Chemical and thermal constraints on focussed fluid flow in the lower oceanic crust. *American Journal of Science*, 306(6), 389–427. <https://doi.org/10.2475/06.2006.01>
- Coogan, L. A., Jenkin, G. R. T., & Wilson, R. N. (2002). Constraining the cooling rate of the lower oceanic crust: A new approach applied to the Oman ophiolite. *Earth and Planetary Science Letters*, 199(1), 127–146. [https://doi.org/10.1016/S0012-821X\(02\)00554-X](https://doi.org/10.1016/S0012-821X(02)00554-X)
- Coogan, L. A., & O'Hara, M. J. (2015). MORB differentiation: In situ crystallization in replenished-tapped magma chambers. *Geochimica et Cosmochimica Acta*, 158, 147–161. <https://doi.org/10.1016/j.gca.2015.03.010>
- Coogan, L. A., Thompson, G., & MacLeod, C. J. (2002). A textural and geochemical investigation of high level gabbros from the Oman ophiolite: Implications for the role of the axial magma chamber at fast-spreading ridges. *Lithos*, 63(1), 67–82. [https://doi.org/10.1016/S0024-4937\(02\)00114-7](https://doi.org/10.1016/S0024-4937(02)00114-7)
- Costa, F., Coogan, L. A., & Chakraborty, S. (2010). The time scales of magma mixing and mingling involving primitive melts and melt–mush interaction at mid-ocean ridges. *Contributions to Mineralogy and Petrology*, 159(3), 371–387. <https://doi.org/10.1007/s00410-009-0432-3>
- Crawford, W. C., & Webb, S. C. (2002). Variations in the distribution of magma in the lower crust and at the Moho beneath the East Pacific Rise at 9°–10°N. *Earth and Planetary Science Letters*, 203(1), 117–130. [https://doi.org/10.1016/S0012-821X\(02\)00831-2](https://doi.org/10.1016/S0012-821X(02)00831-2)

- Crawford, W. C., Webb, S. C., & Hildebrand, J. A. (1999). Constraints on melt in the lower crust and Moho at the East Pacific Rise, 9°48'N, using seafloor compliance measurements. *Journal of Geophysical Research*, 104(B2), 2923–2939. <https://doi.org/10.1029/1998JB900087>
- Curran, A., Wolff, P. E., Koepke, J., Almeev, R. R., Zhang, C., Zühlmann, B., et al. (2018). Chlorine-rich amphibole in deep layered gabbros as evidence for brine/rock interaction in the lower oceanic crust: A case study from the Wadi Wariyah, Samail Ophiolite, Sultanate of Oman. *Lithos*, 323, 125–136. <https://doi.org/10.1016/j.lithos.2018.09.015>
- Detrick, R. S., Buhl, P., Vera, E., Mutter, J., Orcutt, J., Madsen, J., & Brocher, T. (1987). Multi-channel seismic imaging of a crustal magma chamber along the East Pacific Rise. *Nature*, 326(6108), 35–41. <https://doi.org/10.1038/326035a0>
- Dunn, R. A., Toomey, D. R., & Solomon, S. C. (2000). Three-dimensional seismic structure and physical properties of the crust and shallow mantle beneath the East Pacific Rise at 9°30'N. *Journal of Geophysical Research: Solid Earth*, 105(B10), 23537–23555. <https://doi.org/10.1029/2000JB900210>
- Dyger, N., Kelemen, P. B., & Liang, Y. (2017). Spatial variations in cooling rate in the mantle section of the Samail ophiolite in Oman: Implications for formation of lithosphere at mid-ocean ridges. *Earth and Planetary Science Letters*, 465, 134–144. <https://doi.org/10.1016/j.epsl.2017.02.038>
- Faak, K., Chakraborty, S., & Coogan, L. A. (2013). Mg in plagioclase: Experimental calibration of a new geothermometer and diffusion coefficients. *Geochimica et Cosmochimica Acta*, 123, 195–217. <https://doi.org/10.1016/j.gca.2013.05.009>
- Faak, K., Coogan, L. A., & Chakraborty, S. (2015). Near conductive cooling rates in the upper-plutonic section of crust formed at the East Pacific Rise. *Earth and Planetary Science Letters*, 423, 36–47. <https://doi.org/10.1016/j.epsl.2015.04.025>
- Faak, K., & Gillis, K. M. (2016). Slow cooling of the lowermost oceanic crust at the fast-spreading East Pacific Rise. *Geology*, 44(2), 115–118. <https://doi.org/10.1130/G37353.1>
- Feig, S. T., Koepke, J., & Snow, J. E. (2006). Effect of water on tholeiitic basalt phase equilibria: An experimental study under oxidizing conditions. *Contributions to Mineralogy and Petrology*, 152(5), 611–638. <https://doi.org/10.1007/s00410-006-0123-2>
- France, L., Ildefonse, B., & Koepke, J. (2009). Interactions between magma and hydrothermal system in Oman ophiolite and in IODP Hole 1256D: Fossilization of a dynamic melt lens at fast spreading ridges. *Geochemistry, Geophysics, Geosystems*, 10(10), 1–30. <https://doi.org/10.1029/2009GC002652>
- Francheteau, J., Armijo, R., Cheminée, J. L., Hékinian, R., Lonsdale, P., & Blum, N. (1990). 1 Ma East Pacific Rise oceanic crust and uppermost mantle exposed by rifting in Hess Deep (equatorial Pacific Ocean). *Earth and Planetary Science Letters*, 101(2), 281–295. [https://doi.org/10.1016/0012-821X\(90\)90160-Y](https://doi.org/10.1016/0012-821X(90)90160-Y)
- Fricker, M. B., Kutscher, D., Aeschlimann, B., Frommer, J., Dietiker, R., Bettmer, J., & Günther, D. (2011). High spatial resolution trace element analysis by LA-ICP-MS using a novel ablation cell for multiple or large samples. *International Journal of Mass Spectrometry*, 307(1), 39–45. <https://doi.org/10.1016/j.ijms.2011.01.008>
- Gaetani, G. A., Grove, T. L., & Bryan, W. B. (1993). The influence of water on the petrogenesis of subduction related igneous rocks. *Nature*, 365(6444), 332–334. <https://doi.org/10.1038/365332a0>
- Gale, A., Dalton, C. A., Langmuir, C. H., Su, Y., & Schilling, J.-G. (2013). The mean composition of ocean ridge basalts. *Geochemistry, Geophysics, Geosystems*, 14(3), 489–518. <https://doi.org/10.1029/2012GC004334>
- Garbe-Schönberg, C. D. (1993). Simultaneous determination of thirty-seven trace elements in twenty-eight international rock standards by ICP-MS. *Geostandards Newsletter*, 17(1), 81–97. <https://doi.org/10.1111/j.1751-908X.1993.tb00122.x>
- Garbe-Schönberg, D., Koepke, J., Müller, S., Mock, D., Müller, S., & Nasir, S. (2022). A reference section through fast-spread lower oceanic crust, Wadi Gideah, Samail Ophiolite (Sultanate of Oman): Whole rock geochemistry. *Journal of Geophysical Research: Solid Earth*.
- Garbe-Schönberg, D., & Müller, S. (2014). Nano-particulate pressed powder tablets for LA-ICP-MS. *Journal of Analytical Atomic Spectrometry*, 29(6), 990–1000. <https://doi.org/10.1039/C4JA00007B>
- Garrido, C. J., Kelemen, P. B., & Hirth, G. (2001). Variation of cooling rate with depth in lower crust formed at an oceanic spreading ridge: Plagioclase crystal size distributions in gabbros from the Oman ophiolite. *Geochemistry, Geophysics, Geosystems*, 2(10), 1–21. <https://doi.org/10.1029/2000GC000136>
- Ghiorsio, M. S., & Sack, R. O. (1995). Chemical mass transfer in magmatic processes IV. A revised and internally consistent thermodynamic model for the interpolation and extrapolation of liquid-solid equilibria in magmatic systems at elevated temperatures and pressures. *Contributions to Mineralogy and Petrology*, 119(2), 197–212. <https://doi.org/10.1007/BF00307281>
- Gillis, K. M., Snow, J. E., Klaus, A., Abe, N., Adrião, Á. B., Akizawa, N., et al. (2014). Primitive layered gabbros from fast-spreading lower oceanic crust. *Nature*, 505(7482), 204–207. <https://doi.org/10.1038/nature12778>
- Glennie, K. W., Boeuf, M. G. A., Clarke, M. W. H., Moody-Stuart, M., Pilaar, W. F. H., & Reinhardt, B. M. (1973). Late Cretaceous nappes in Oman Mountains and their geologic evolution. *AAPG Bulletin*, 57(1), 5–27. <https://doi.org/10.1306/819A4240-16C5-11D7-8645000102C1865D>
- Godard, M., Dautria, J.-M., & Perrin, M. (2003). Geochemical variability of the Oman ophiolite lavas: Relationship with spatial distribution and paleomagnetic directions. *Geochemistry, Geophysics, Geosystems*, 4(6), 1–15. <https://doi.org/10.1029/2002GC000452>
- Goodenough, K. M., Styles, M. T., Schofield, D., Thomas, R. J., Crowley, Q. C., Lilly, R. M., et al. (2010). Architecture of the Oman–UAE ophiolite: Evidence for a multi-phase magmatic history. *Arabian Journal of Geosciences*, 3(4), 439–458. <https://doi.org/10.1007/s12517-010-0177-3>
- Goodenough, K. M., Thomas, R. J., Styles, M. T., Schofield, D. I., & MacLeod, C. J. (2014). Records of ocean growth and destruction in the Oman–UAE ophiolite. *Elements*, 10(2), 109–114. <https://doi.org/10.2113/gselements.10.2.109>
- Govindaraju, K. (1995). 1995 Working values with confidence limits for twenty-six CRPG, ANRT and IWG-GIT geostandards. *Geostandards Newsletter*, 19(S1), 1–32. <https://doi.org/10.1111/j.1751-908X.1995.tb00164.x>
- Gregory, R. T., & Taylor, H. P. (1981). An oxygen isotope profile in a section of Cretaceous oceanic crust, Samail Ophiolite, Oman: Evidence for $\delta^{18}\text{O}$ buffering of the oceans by deep (>5 km) seawater-hydrothermal circulation at mid-ocean ridges. *Journal of Geophysical Research*, 86(B4), 2737–2755. <https://doi.org/10.1029/JB086iB04p02737>
- Guilmette, C., Smit, M. A., van Hinsbergen, D. J. J., Gürer, D., Corfu, F., Charette, B., et al. (2018). Forced subduction initiation recorded in the sole and crust of the Samail Ophiolite of Oman. *Nature Geoscience*, 11(9), 688–695. <https://doi.org/10.1038/s41561-018-0209-2>
- Hack, P. J., Nielsen, R. L., & Johnston, A. D. (1994). Experimentally determined rare-earth element and Y partitioning behavior between clinopyroxene and basaltic liquids at pressures up to 20 kbar. *Chemical Geology*, 117(1), 89–105. [https://doi.org/10.1016/0009-2541\(94\)90123-6](https://doi.org/10.1016/0009-2541(94)90123-6)
- Han, S., Carbotte, S. M., Carton, H., Mutter, J. C., Aghaei, O., Nedimović, M. R., & Canales, J. P. (2014). Architecture of on- and off-axis magma bodies at EPR 9°37'–40'N and implications for oceanic crustal accretion. *Earth and Planetary Science Letters*, 390, 31–44. <https://doi.org/10.1016/j.epsl.2013.12.040>
- Hasenclever, J., Theissen-Krah, S., Rüpke, L. H., Morgan, J. P., Iyer, K., Petersen, S., & Devey, C. W. (2014). Hybrid shallow on-axis and deep off-axis hydrothermal circulation at fast-spreading ridges. *Nature*, 508(7497), 508–512. <https://doi.org/10.1038/nature13174>
- Henstock, T. J., Woods, A. W., & White, R. S. (1993). The accretion of oceanic crust by episodic sill intrusion. *Journal of Geophysical Research*, 98(B3), 4143–4161. <https://doi.org/10.1029/92JB02661>

- Hopson, C. A. (2007). Subvolcanic sheeted sills and nonsheeted dikes in ophiolites: Occurrence, origin, and tectonic significance for oceanic crust generation. In M. Cloos, W. D. Carlson, M. C. Gilbert, J. G. Liou, & S. S. Sorensen (Eds.), *Convergent margin terranes and associated regions: A tribute to W.G. Ernst* (Vol. 419, pp. 0–254). Geological Society of America. [https://doi.org/10.1130/2006.2419\(12\)](https://doi.org/10.1130/2006.2419(12))
- Hopson, C. A., Coleman, R. G., Gregory, R. T., Pallister, J. S., & Bailey, E. H. (1981). Geologic section through the Samail ophiolite and associated rocks along a Muscat-Ibra transect, southeastern Oman Mountains. *Journal of Geophysical Research*, 86(B4), 2527–2544. <https://doi.org/10.1029/JB086iB04p02527>
- Hussenöeder, S. A., Collins, J. A., Kent, G. M., & Detrick, R. S. (1996). Seismic analysis of the axial magma chamber reflector along the southern East Pacific Rise from conventional reflection profiling. *Journal of Geophysical Research*, 101(B10), 22087–22105. <https://doi.org/10.1029/96JB01907>
- Imai, N., Terashima, S., Itoh, S., & Ando, A. (1995). 1994 Compilation of analytical data for minor and trace elements in seventeen GSI geochemical reference samples, “Igneous Rock Series”. *Geostandards Newsletter*, 19(2), 135–213. <https://doi.org/10.1111/j.1751-908X.1995.tb00158.x>
- Jochum, K. P., & Jenner, G. (1994). Trace element analysis of Geological Survey of Japan silicate reference materials: Comparison of SSMS with ICP-MS data and a critical discussion of compiled values. *Fresenius' Journal of Analytical Chemistry*, 350(4), 310–318. <https://doi.org/10.1007/BF00322488>
- Jochum, K. P., Nohl, U., Herwig, K., Lammel, E., Stoll, B., & Hofmann, A. W. (2005). GeoReM: A new geochemical database for reference materials and isotopic standards. *Geostandards Newsletter*, 29(3), 333–338. <https://doi.org/10.1111/j.1751-908X.2005.tb00904.x>
- Jochum, K. P., Stoll, B., Herwig, K., Willbold, M., Hofmann, A. W., Amini, M., et al. (2006). MPI-DING reference glasses for in situ microanalysis: New reference values for element concentrations and isotope ratios. *Geochemistry, Geophysics, Geosystems*, 7(2), 1–44. <https://doi.org/10.1029/2005GC001060>
- Jochum, K. P., Weis, U., Schwager, B., Stoll, B., Wilson, S. A., Haug, G. H., et al. (2016). Reference values following ISO guidelines for frequently requested rock reference materials. *Geostandards and Geoanalytical Research*, 40(3), 333–350. <https://doi.org/10.1111/j.1751-908X.2015.00392.x>
- Jochum, K. P., Willbold, M., Raczek, I., Stoll, B., & Herwig, K. (2005). Chemical characterisation of the USGS reference glasses GSA-1G, GSC-1G, GSD-1G, GSE-1G, BCR-2G, BHVO-2G and BIR-1G using EPMA, ID-TIMS, ID-ICP-MS and LA-ICP-MS. *Geostandards and Geoanalytical Research*, 29(3), 285–302. <https://doi.org/10.1111/j.1751-908X.2005.tb00901.x>
- Jousselin, D., Morales, L. F. G., Nicolle, M., & Stephant, A. (2012). Gabbro layering induced by simple shear in the Oman ophiolite Moho transition zone. *Earth and Planetary Science Letters*, 331–332, 55–66. <https://doi.org/10.1016/j.epsl.2012.02.022>
- Kelemen, P. B., & Aharonov, E. (1998). Periodic formation of magma fractures and generation of layered gabbros in the lower crust beneath oceanic spreading ridges. In W. Roger Buck, P. T. Delaney, J. A. Karson, & Y. Lagabriele (Eds.), *Faulting and magmatism at mid-ocean ridges* (Vol. 100, pp. 267–289). American Geophysical Union. <https://doi.org/10.1029/GM106p0267>
- Kelemen, P. B., Hirth, G., Shimizu, N., Spiegelman, M., & Dick, H. J. (1997). A review of melt migration processes in the adiabatically upwelling mantle beneath oceanic spreading ridges. *Philosophical Transactions of the Royal Society of London. Series A: Mathematical, Physical and Engineering Sciences*, 355(1723), 283–318. <https://doi.org/10.1098/rsta.1997.0010>
- Kelemen, P. B., Koga, K., & Shimizu, N. (1997). Geochemistry of gabbro sills in the crust-mantle transition zone of the Oman ophiolite: Implications for the origin of the oceanic lower crust. *Earth and Planetary Science Letters*, 146(3), 475–488. [https://doi.org/10.1016/S0012-821X\(96\)00235-X](https://doi.org/10.1016/S0012-821X(96)00235-X)
- Kelemen, P. B., Matter, J. M., Teagle, D. A. H., Coggon, J. A., & the Oman Drilling Project Science Team. (2020a). Site GT1: Layered cumulate gabbros and deep fault zones. In P. B. Kelemen, J. M. Matter, D. A. H. Teagle, J. A. Coggon, & the Oman Drilling Project Science Team (Eds.), *Proceedings of the Oman Drilling Project: College Station, TX (International Ocean Discovery Program)*. <https://doi.org/10.14379/OmanDP.proc.2020>
- Kelemen, P. B., Matter, J. M., Teagle, D. A. H., Coggon, J. A., & the Oman Drilling Project Science Team. (2020b). Site GT2: Foliated to layered gabbro transition. In P. B. Kelemen, J. M. Matter, D. A. H. Teagle, J. A. Coggon, & the Oman Drilling Project Science Team (Eds.), *Proceedings of the Oman Drilling Project: College Station, TX (International Ocean Discovery Program)*. <https://doi.org/10.14379/OmanDP.proc.2020>
- Kent, G. M., Singh, S. C., Harding, A. J., Sinha, M. C., Orcutt, J. A., Barton, P. J., et al. (2000). Evidence from three-dimensional seismic reflectivity images for enhanced melt supply beneath mid-ocean ridge discontinuities. *Nature*, 406(6796), 614–618. <https://doi.org/10.1038/35020543>
- Kinzler, R. J., & Grove, T. L. (1993). Corrections and further discussion of the primary magmas of mid-ocean ridge basalts, 1 and 2. *Journal of Geophysical Research*, 98(B12), 22339–22347. <https://doi.org/10.1029/93JB02164>
- Koepke, J., Berndt, J., Horn, I., Fahle, J., & Wolff, P. E. (2014). Partial melting of oceanic gabbro triggered by migrating water-rich fluids: A prime example from the Oman ophiolite. *Geological Society, London, Special Publications*, 392(1), 195–212. <https://doi.org/10.1144/SP392.10>
- Koepke, J., Feig, S. T., Berndt, J., & Neave, D. A. (2021). Wet magmatic processes during the accretion of the deep crust of the Oman Ophiolite paleoridge: Phase diagrams and petrological records. *Tectonophysics*, 817, 229051. <https://doi.org/10.1016/j.tecto.2021.229051>
- Koepke, J., Feig, S. T., & Snow, J. (2005a). Hydrous partial melting within the lower oceanic crust. *Terra Nova*, 17(3), 286–291. <https://doi.org/10.1111/j.1365-3121.2005.00613.x>
- Koepke, J., Feig, S. T., & Snow, J. (2005b). Late stage magmatic evolution of oceanic gabbros as a result of hydrous partial melting: Evidence from the Ocean Drilling Program (ODP) Leg 153 drilling at the Mid-Atlantic Ridge. *Geochemistry, Geophysics, Geosystems*, 6(2), 1–27. <https://doi.org/10.1029/2004GC000805>
- Koepke, J., Feig, S. T., Snow, J., & Freise, M. (2004). Petrogenesis of oceanic plagiogranites by partial melting of gabbros: An experimental study. *Contributions to Mineralogy and Petrology*, 146(4), 414–432. <https://doi.org/10.1007/s00410-003-0511-9>
- Koepke, J., France, L., Müller, T., Faure, F., Goetze, N., Dziony, W., & Ildefonse, B. (2011). Gabbros from IODP Site 1256, equatorial Pacific: Insight into axial magma chamber processes at fast spreading ocean ridges. *Geochemistry, Geophysics, Geosystems*, 12(9), 1–28. <https://doi.org/10.1029/2011GC003655>
- Koepke, J., Garbe-Schoenberg, C. D., Müller, T., Mueller, S., Mock, D., Strauss, H., et al. (2017). A reference section through the lower fast-spreading oceanic crust in the Wadi Gideah (Sumail ophiolite, Sultanate Oman): Drill sites GT1A and GT2A within the ICDP Oman Drilling Project. In *Paper presented at the AGU Fall Meeting Abstracts* (Vol. 2017, pp. V43G–2957).
- Koepke, J., Garbe-Schoenberg, C. D., Müller, T., Mock, D., Müller, S., & Nasir, S. (2022). A reference section through fast-spread lower oceanic crust, Wadi Gideah, Samail Ophiolite (Sultanate of Oman): Petrography and petrology. *Journal of Geophysical Research: Solid Earth*, 127(1), 1–35. <https://doi.org/10.1029/2021JB022735>

- Koepke, J., Mueller, T., Linsler, S., Schuth, S., Garbe-Schoenberg, C. D., & McCaig, A. M. (2014). Invasion of seawater-derived fluids at very high temperatures in the Oman ophiolite - A key for cooling the deep crust at fast-spreading ridges. In *Paper presented at the AGU Fall Meeting Abstracts, San Francisco* (Vol. 2014, pp. V23E-03).
- Koepke, J., Schoenborn, S., Oelze, M., Wittmann, H., Feig, S. T., Hellebrand, E., et al. (2009). Petrogenesis of crustal wehrlites in the Oman ophiolite: Experiments and natural rocks. *Geochemistry, Geophysics, Geosystems*, 10(10), 1–26. <https://doi.org/10.1029/2009GC002488>
- Korenaga, J., & Kelemen, P. B. (1997). Origin of gabbro sills in the Moho transition zone of the Oman ophiolite: Implications for magma transport in the oceanic lower crust. *Journal of Geophysical Research*, 102(B12), 27729–27749. <https://doi.org/10.1029/97JB02604>
- Korenaga, J., & Kelemen, P. B. (1998). Melt migration through the oceanic lower crust: A constraint from melt percolation modeling with finite solid diffusion. *Earth and Planetary Science Letters*, 156(1), 1–11. [https://doi.org/10.1016/S0012-821X\(98\)00004-1](https://doi.org/10.1016/S0012-821X(98)00004-1)
- Kurosawa, M., Shima, K., Ishii, S., & Sasa, K. (2006). Trace element analysis of fused whole-rock glasses by laser ablation-ICP-MS and PIXE. *Geostandards and Geoanalytical Research*, 30(1), 17–30. <https://doi.org/10.1111/j.1751-908X.2006.tb00908.x>
- Lambart, S., Koornneef, J. M., Millet, M.-A., Davies, G. R., Cook, M., & Lissenberg, C. J. (2019). Highly heterogeneous depleted mantle recorded in the lower oceanic crust. *Nature Geoscience*, 12(6), 482–486. <https://doi.org/10.1038/s41561-019-0368-9>
- Langmuir, C. H. (1989). Geochemical consequences of in situ crystallization. *Nature*, 340(6230), 199–205. <https://doi.org/10.1038/340199a0>
- Langmuir, C. H., & Forsyth, D. W. (2007). Mantle melting beneath mid-ocean ridges. *Oceanography*, 20(1), 78–89. <https://doi.org/10.2307/24859977>
- Lanphere, M. A., Coleman, R. G., & Hopson, C. A. (1981). Sr isotopic tracer study of the Samail ophiolite, Oman. *Journal of Geophysical Research*, 86(B4), 2709–2720. <https://doi.org/10.1029/JB086iB04p02709>
- Liang, Y., Sun, C., & Yao, L. (2013). A REE-in-two-pyroxene thermometer for mafic and ultramafic rocks. *Geochimica et Cosmochimica Acta*, 102, 246–260. <https://doi.org/10.1016/j.gca.2012.10.035>
- Lissenberg, C. J., & MacLeod, C. J. (2016). A reactive porous flow control on mid-ocean ridge magmatic evolution. *Journal of Petrology*, 57(11–12), 2195–2220. <https://doi.org/10.1093/ptrology/egw074>
- Lissenberg, C. J., MacLeod, C. J., Howard, K. A., & Godard, M. (2013). Pervasive reactive melt migration through fast-spreading lower oceanic crust (Hess Deep, equatorial Pacific Ocean). *Earth and Planetary Science Letters*, 361, 436–447. <https://doi.org/10.1016/j.epsl.2012.11.012>
- MacLennan, J., Hulme, T., & Singh, S. C. (2004). Thermal models of oceanic crustal accretion: Linking geophysical, geological and petrological observations. *Geochemistry, Geophysics, Geosystems*, 5(2), 1–32. <https://doi.org/10.1029/2003GC000605>
- MacLennan, J., Hulme, T., & Singh, S. C. (2005). Cooling of the lower oceanic crust. *Geology*, 33(5), 357–366. <https://doi.org/10.1130/G21207.1>
- MacLeod, C. J., Lissenberg, C. J., & Bibby, L. E. (2013). “Moist MORB” axial magmatism in the Oman ophiolite: The evidence against a mid-ocean ridge origin. *Geology*, 41(4), 459–462. <https://doi.org/10.1130/G33904.1>
- MacLeod, C. J., & Yaouancq, G. (2000). A fossil melt lens in the Oman ophiolite: Implications for magma chamber processes at fast spreading ridges. *Earth and Planetary Science Letters*, 176(3), 357–373. [https://doi.org/10.1016/S0012-821X\(00\)00020-0](https://doi.org/10.1016/S0012-821X(00)00020-0)
- Maher, S. M., Gee, J. S., Cheadle, M. J., & John, B. E. (2021). Three-dimensional magnetic stripes require slow cooling in fast-spread lower ocean crust. *Nature*, 597(7877), 511–515. <https://doi.org/10.1038/s41586-021-03831-6>
- Marjanović, M., Carbotte, S. M., Carton, H., Nedimović, M. R., Mutter, J. C., & Canales, J. P. (2014). A multi-sill magma plumbing system beneath the axis of the East Pacific Rise. *Nature Geoscience*, 7(11), 825–829. <https://doi.org/10.1038/ngeo2272>
- McDonough, W. F., & Sun, S.-S. (1995). The composition of the Earth. *Chemical Geology*, 120(3), 223–253. [https://doi.org/10.1016/0009-2541\(94\)00140-4](https://doi.org/10.1016/0009-2541(94)00140-4)
- Mock, D., Ildefonse, B., Müller, T., & Koepke, J. (2021). A reference section through fast-spread lower oceanic crust, Wadi Gideah, Samail Ophiolite (Sultanate of Oman): Insights from Crystallographic Preferred Orientations. *Journal of Geophysical Research: Solid Earth*, 126(6), 1–27. <https://doi.org/10.1029/2021JB021864>
- Mock, D., Neave, D. A., Müller, S., Garbe-Schönberg, D., Namur, O., Ildefonse, B., & Koepke, J. (2021). Formation of igneous layering in the lower oceanic crust from the Samail Ophiolite, Sultanate of Oman. *Journal of Geophysical Research: Solid Earth*, 126(1), e2020JB019573. <https://doi.org/10.1029/2020JB019573>
- Morse, S. A. (2010). A critical comment on Thy et al. (2009b): Liquidus temperatures of the Skaergaard magma. *American Mineralogist*, 95(11–12), 1817–1827. <https://doi.org/10.2138/am.2010.3473>
- Mueller, S. (2021). thewoodsofcode/pl-cpx-REE-T: pl-cpx-REE-T v1.0.0 (v1.0.0). *Zenodo*. <https://doi.org/10.5281/zenodo.5702687>
- Müller, S., Garbe-Schönberg, D., Koepke, J., & Hoernle, K. (2021). Petrographic key parameter, EPMA data, LA-ICP-MS data, for plagioclase and clinopyroxene of 39 gabbro samples from the Oman Ophiolite (Wadi Gideah Transect). *PANGAEA*. <https://doi.org/10.1594/PANGAEA.934706>
- Müller, T. (2015). *A petrological and geochemical cross section of lower crust at the Wadi Gideah (Samail ophiolite): Implications for the crustal accretion at fast-spreading mid-ocean ridges* (Doctoral dissertation). Université de Montpellier & Hannover University. <https://doi.org/10.15488/8750>
- Müller, T., Koepke, J., Garbe-Schönberg, C. D., Dietrich, M., Bauer, U., & Wolff, P. E. (2017). Anatomy of a frozen axial melt lens from a fast-spreading paleo-ridge (Wadi Gideah, Oman ophiolite). *Lithos*, 272–273, 31–45. <https://doi.org/10.1016/j.lithos.2016.11.022>
- Nicolas, A., & Boudier, F. (2015). Inside the magma chamber of a dying ridge segment in the Oman ophiolite. *Terra Nova*, 27(1), 69–76. <https://doi.org/10.1111/ter.12130>
- Nicolas, A., Boudier, F., & France, L. (2009). Subsidence in magma chamber and the development of magmatic foliation in Oman ophiolite gabbros. *Earth and Planetary Science Letters*, 284(1), 76–87. <https://doi.org/10.1016/j.epsl.2009.04.012>
- Nicolas, A., Boudier, F., Ildefonse, B., & Ball, E. (2000). Accretion of Oman and United Arab Emirates ophiolite – Discussion of a new structural map. *Marine Geophysical Researches*, 21(3), 147–180. <https://doi.org/10.1023/A:1026769727917>
- Nicolas, A., Boudier, F., Koepke, J., France, L., Ildefonse, B., & Mevel, C. (2008). Root zone of the sheeted dike complex in the Oman ophiolite. *Geochemistry, Geophysics, Geosystems*, 9(5), 1–29. <https://doi.org/10.1029/2007GC001918>
- Nicolas, A., & Mainprice, D. (2005). Burst of high-temperature seawater injection throughout accreting oceanic crust: A case study in Oman ophiolite. *Terra Nova*, 17(4), 326–330. <https://doi.org/10.1111/j.1365-3121.2005.00617.x>
- Nicolas, A., Mainprice, D., & Boudier, F. (2003). High-temperature seawater circulation throughout crust of oceanic ridges: A model derived from the Oman ophiolites. *Journal of Geophysical Research: Solid Earth*, 108(B8), 2371. <https://doi.org/10.1029/2002JB002094>
- Oeser, M., Strauss, H., Wolff, P. E., Koepke, J., Peters, M., Garbe-Schönberg, C. D., & Dietrich, M. (2012). A profile of multiple sulfur isotopes through the Oman ophiolite. *Chemical Geology*, 312–313, 27–46. <https://doi.org/10.1016/j.chemgeo.2012.04.008>
- O'Hara, M. J., & Fry, N. (1996). Geochemical effects of small packet crystallization in large magma chambers—Further resolution of the highly compatible element paradox. *Journal of Petrology*, 37(4), 891–925. <https://doi.org/10.1093/ptrology/37.4.891>
- O'Hara, M. J., & Mathews, R. E. (1981). Geochemical evolution in an advancing, periodically replenished, periodically tapped, continuously fractionated magma chamber. *Journal of the Geological Society*, 138(3), 237–277. <https://doi.org/10.1144/gsjgs.138.3.0237>

- Pallister, J. S., & Hopson, C. A. (1981). Samail ophiolite plutonic suite: Field relations, phase variation, cryptic variation and layering, and a model of a spreading ridge magma chamber. *Journal of Geophysical Research*, 86(B4), 2593–2644. <https://doi.org/10.1029/JB086iB04p02593>
- Pallister, J. S., & Knight, R. J. (1981). Rare-earth element geochemistry of the Samail ophiolite near Ibra, Oman. *Journal of Geophysical Research*, 86(B4), 2673–2697. <https://doi.org/10.1029/JB086iB04p02673>
- Pedersen, R. B., Malpas, J., & Falloon, T. (1996). Petrology and geochemistry of gabbroic and related rocks from site 894, Hess Deep. In C. Mével, K. M. Gillis, J. F. Allan, & P. S. Meyer (Eds.), *Proceedings of the Ocean Drilling Program* (Vol. 147, pp. 3–20).
- Perfit, M. R., & Chadwick, W., Jr. (1998). Magmatism at mid-ocean ridges: Constraints from volcanological and geochemical investigations. In W. Roger Buck, P. T. Delaney, J. A. Karson, & Y. Lagabriele (Eds.), *Faulting and magmatism at mid-ocean ridges* (Vol. 106, pp. 59–115). American Geophysical Union (AGU). <https://doi.org/10.1029/GM106p0059>
- Perk, N. W., Coogan, L. A., Karson, J. A., Klein, E. M., & Hanna, H. D. (2007). Petrology and geochemistry of primitive lower oceanic crust from Pito Deep: Implications for the accretion of the lower crust at the Southern East Pacific Rise. *Contributions to Mineralogy and Petrology*, 154(5), 575–590. <https://doi.org/10.1007/s00410-007-0210-z>
- Peters, T., Amin, El O., Blechschmid, I., & Al-Busaidi, S. (2008). *Geological map of Oman 1:50000, sheet NF 40-8A1*. Sultanate of Oman Ministry of Commerce and Industry.
- Pouchou, J. L., & Pichoir, F. (1991). Quantitative analysis of homogeneous or stratified microvolumes applying the model “PAP”. In K. F. J. Heinrich & D. E. Newbury (Eds.), *Electron probe quantitation* (pp. 31–75). Springer. https://doi.org/10.1007/978-1-4899-2617-3_4
- Putirka, K. D. (2005). Igneous thermometers and barometers based on plagioclase + liquid equilibria: Tests of some existing models and new calibrations. *American Mineralogist*, 90(2–3), 336–346. <https://doi.org/10.2138/am.2005.1449>
- Putirka, K. D. (2008). Thermometers and barometers for volcanic systems. *Reviews in Mineralogy and Geochemistry*, 69(1), 61–120. <https://doi.org/10.2138/rmg.2008.69.3>
- Quick, J. E., & Denlinger, R. P. (1993). Ductile deformation and the origin of layered gabbro in ophiolites. *Journal of Geophysical Research*, 98(B8), 14015–14027. <https://doi.org/10.1029/93JB00698>
- Rioux, M., Bowring, S., Kelemen, P. B., Gordon, S., Dudas, F., & Miller, R. (2012). Rapid crustal accretion and magma assimilation in the Oman-U.A.E. ophiolite: High precision U-Pb zircon geochronology of the gabbroic crust. *Journal of Geophysical Research: Solid Earth*, 117(B7), 1–12. <https://doi.org/10.1029/2012JB009273>
- Rospabé, M., Ceuleneer, G., Benoit, M., Abily, B., & Pinet, P. (2017). Origin of the dunitic mantle-crust transition zone in the Oman ophiolite: The interplay between percolating magmas and high-temperature hydrous fluids. *Geology*, 45(5), 471–474. <https://doi.org/10.1130/G38778.1>
- Searle, M., & Cox, J. (1999). Tectonic setting, origin, and obduction of the Oman ophiolite. *GSA Bulletin*, 111(1), 104–122. [https://doi.org/10.1130/0016-7606\(1999\)111<0104:TSAOO>2.3.CO;2](https://doi.org/10.1130/0016-7606(1999)111<0104:TSAOO>2.3.CO;2)
- Singh, S. C., Collier, J. S., Harding, A. J., Kent, G. M., & Orcutt, J. A. (1999). Seismic evidence for a hydrothermal layer above the solid roof of the axial magma chamber at the southern East Pacific Rise. *Geology*, 27(3), 219–222. [https://doi.org/10.1130/0091-7613\(1999\)027<0219:SEFAHL>2.3.CO;2](https://doi.org/10.1130/0091-7613(1999)027<0219:SEFAHL>2.3.CO;2)
- Sinton, J. M., & Detrick, R. S. (1992). Mid-ocean ridge magma chambers. *Journal of Geophysical Research*, 97(B1), 197–216. <https://doi.org/10.1029/91JB02508>
- Sobolev, A. V., & Shimizu, N. (1993). Ultra-depleted primary melt included in an olivine from the Mid-Atlantic Ridge. *Nature*, 363(6425), 151–154. <https://doi.org/10.1038/363151a0>
- Sun, C., Graff, M., & Liang, Y. (2017). Trace element partitioning between plagioclase and silicate melt: The importance of temperature and plagioclase composition, with implications for terrestrial and lunar magmatism. *Geochimica et Cosmochimica Acta*, 206, 273–295. <https://doi.org/10.1016/j.gca.2017.03.003>
- Sun, C., & Liang, Y. (2017). A REE-in-plagioclase-clinopyroxene thermometer for crustal rocks. *Contributions to Mineralogy and Petrology*, 172(4), 24. <https://doi.org/10.1007/s00410-016-1326-9>
- Sun, C., & Lissenberg, C. J. (2018). Formation of fast-spreading lower oceanic crust as revealed by a new Mg–REE coupled geospeedometer. *Earth and Planetary Science Letters*, 487, 165–178. <https://doi.org/10.1016/j.epsl.2018.01.032>
- Theissen-Krah, S., Iyer, K., Rüpke, L. H., & Morgan, J. P. (2011). Coupled mechanical and hydrothermal modeling of crustal accretion at intermediate to fast spreading ridges. *Earth and Planetary Science Letters*, 311(3), 275–286. <https://doi.org/10.1016/j.epsl.2011.09.018>
- Theissen-Krah, S., Rüpke, L. H., & Hasenclever, J. (2016). Modes of crustal accretion and their implications for hydrothermal circulation. *Geophysical Research Letters*, 43(3), 1124–1131. <https://doi.org/10.1002/2015GL067335>
- Thy, P., Leshner, C. E., & Tegner, C. (2008). The Skaergaard liquid line of descent revisited. *Contributions to Mineralogy and Petrology*, 157(6), 735–747. <https://doi.org/10.1007/s00410-008-0361-6>
- Thy, P., Tegner, C., & Leshner, C. E. (2009). Liquidus temperatures of the Skaergaard magma. *American Mineralogist*, 94(10), 1371–1376. <https://doi.org/10.2138/am.2009.3058>
- VanTongeren, J. A., Hirth, G., & Kelemen, P. B. (2015). Constraints on the accretion of the gabbroic lower oceanic crust from plagioclase lattice preferred orientation in the Samail ophiolite. *Earth and Planetary Science Letters*, 427, 249–261. <https://doi.org/10.1016/j.epsl.2015.07.001>
- VanTongeren, J. A., Kelemen, P. B., Garrido, C. J., Godard, M., Hanghøj, K., Braun, M., & Pearce, J. A. (2021). The composition of the Lower Oceanic crust in the Wadi Khafifah section of the southern Samail (Oman) ophiolite. *Journal of Geophysical Research: Solid Earth*, 126(11), e2021JB021986. <https://doi.org/10.1029/2021JB021986>
- VanTongeren, J. A., Kelemen, P. B., & Hanghøj, K. (2008). Cooling rates in the lower crust of the Oman ophiolite: Ca in olivine, revisited. *Earth and Planetary Science Letters*, 267(1–2), 69–82. <https://doi.org/10.1016/j.epsl.2007.11.034>
- VanTongeren, J. A., & Mathez, E. A. (2013). Incoming magma composition and style of recharge below the Pyroxenite Marker, Eastern Bushveld Complex, South Africa. *Journal of Petrology*, 54(8), 1585–1605. <https://doi.org/10.1093/petrology/egt024>
- Venables, W. N., & Ripley, B. D. (2002). *Modern applied statistics with S* (pp. 1–495). Springer. <https://doi.org/10.1007/978-0-387-21706-2>
- Wanless, V. D., & Shaw, A. M. (2012). Lower crustal crystallization and melt evolution at mid-ocean ridges. *Nature Geoscience*, 5(9), 651–655. <https://doi.org/10.1038/ngeo1552>
- Wilcock, W. S. D., Solomon, S. C., Purdy, G. M., & Toomey, D. R. (1992). The seismic attenuation structure of a fast-spreading mid-ocean ridge. *Science*, 258(5087), 1470–1474. <https://doi.org/10.1126/science.258.5087.1470>
- Wilson, D. S., Teagle, D. A. H., Alt, J. C., Banerjee, N. R., Umino, S., Miyashita, S., et al. (2006). Drilling to gabbro in intact ocean crust. *Science*, 312(5776), 1016–1020. <https://doi.org/10.1126/science.1126090>
- Wolff, P. E., Koepke, J., & Feig, S. T. (2013). The reaction mechanism of fluid-induced partial melting of gabbro in the oceanic crust. *European Journal of Mineralogy*, 25(3), 279–298. <https://doi.org/10.1127/0935-1221/2013/0025-2314>
- Yang, A. Y., Wang, C., Liang, Y., & Lissenberg, C. J. (2019). Reaction between mid-ocean ridge basalt and lower oceanic crust: An experimental study. *Geochemistry, Geophysics, Geosystems*, 20(9), 4390–4407. <https://doi.org/10.1029/2019GC008368>

- Zha, Y., Webb, S. C., Nooner, S. L., & Crawford, W. C. (2014). Spatial distribution and temporal evolution of crustal melt distribution beneath the East Pacific Rise at 9°–10°N inferred from 3-D seafloor compliance modeling. *Journal of Geophysical Research: Solid Earth*, 119(6), 4517–4537. <https://doi.org/10.1002/2014JB011131>
- Zihlmann, B., Müller, S., Coggon, R. M., Koepke, J., Garbe-Schönberg, C. D., & Teagle, D. A. H. (2018). Hydrothermal fault zones in the lower oceanic crust: An example from Wadi Gideah, Samail ophiolite, Oman. *Lithos*, 323, 103–124. <https://doi.org/10.1016/j.lithos.2018.09.008>